Multiscale Magnetosphere-Ionosphere Coupling During Stormtime: A Case Study of the Dawnside Current Wedge

K A Sorathia[1], A Michael[1], V G Merkin[1], S Ohtani[1], A M Keesee[2,3], A Sciola[1], D Lin[4], J Garretson[1], A Y Ukhorskiy[1], S Bao[3], C B Roedig[5], and A Pulkkinen[6]

[1]The Johns Hopkins University Applied Physics Laboratory
[2]Department of Physics and Astronomy, University of New Hampshire
[3]Department of Physics and Astronomy, Rice University
[4]High Altitude Observatory, National Center for Atmospheric Research
[5]VSC-Research Center, Technische Universit at Wien
[6]NASA Goddard Space Flight Center

September 30, 2023

Abstract

A characteristic feature of the main phase of geomagnetic storms is the dawn-dusk asymmetric depression of low- and mid-latitude ground magnetic fields, with largest depression in the dusk sector. Recent work has shown, using data taken from hundreds of storms, that this dawn-dusk asymmetry is strongly correlated with enhancements of the dawnside westward electrojet and this has been interpreted as a 'dawnside current wedge' (DCW). Its ubiquity suggests it is an important aspect of stormtime magnetosphere-ionosphere (MI) coupling. In this work we simulate a moderate geomagnetic storm to investigate the mechanisms that give rise to the formation of the DCW. Using synthetic SuperMAG indices we show that the model reproduces the observed phenomenology of the DCW, namely the correlation between asymmetry in the low-latitude ground perturbation and the dawnside high-latitude ground perturbation. We further show that these periods are characterized by the penetration of mesoscale bursty bulk flows (BBFs) into the dawnside inner magnetosphere. In the context of this event we find that the development of the asymmetric ring current, which inflates the dusk-side magnetotail, leads to asymmetric reconnection and dawnward-biased flow bursts. This results in an eastward expansion and multiscale enhancement of the dawnside electrojet. The electrojet enhancement extends across the dawn quadrant with localized enhancements associated with the wedgelet current systems of the penetrating BBFs. Finally, we connect this work with recent studies that have shown rapid, localized ground variability on the dawnside which can lead to hazardous geomagnetically induced currents.

Multiscale Magnetosphere-Ionosphere Coupling During Stormtime: A Case Study of the Dawnside Current Wedge

K.A. Sorathia[1], A. Michael[1], V.G. Merkin[1], S. Ohtani[1], A.M. Keesee[2], A. Sciola[1], D. Lin[3], J. Garretson[1], A.Y. Ukhorskiy[1], S. Bao[4], C.B. Roedig[5], A. Pulkkinen[6]

[1]The Johns Hopkins University Applied Physics Laboratory, Laurel, MD, USA
[2]Department of Physics and Astronomy, University of New Hampshire, Durham, NH, USA
[3]High Altitude Observatory, National Center for Atmospheric Research, Boulder, CO, USA
[4]Department of Physics and Astronomy, Rice University, Houston, TX, USA
[5]VSC-Research Center,Technische Universit at Wien, Vienna, Austria
[6]NASA Goddard Space Flight Center, Greenbelt, Maryland, USA

Key Points:

- Global model reproduces correlation between ring current asymmetry and dawnside electrojet inferred from hundreds of geomagnetic storms.
- Analysis of the model reveals a dawnside current wedge mediated by mesoscale flow bursts and driven by an asymmetric substorm-like process.
- Model reveals multiscale enhancement of dawnside electrojet with space weather implications due to rapid, localized ground variability.

Corresponding author: Kareem Sorathia, `kareem.sorathia@gmail.com`

Abstract

A characteristic feature of the main phase of geomagnetic storms is the dawn-dusk asymmetric depression of low- and mid-latitude ground magnetic fields, with largest depression in the dusk sector. Recent work has shown, using data taken from hundreds of storms, that this dawn-dusk asymmetry is strongly correlated with enhancements of the dawnside westward electrojet and this has been interpreted as a 'dawnside current wedge' (DCW). Its ubiquity suggests it is an important aspect of stormtime magnetosphere-ionosphere (MI) coupling. In this work we simulate a moderate geomagnetic storm to investigate the mechanisms that give rise to the formation of the DCW. Using synthetic SuperMAG indices we show that the model reproduces the observed phenomenology of the DCW, namely the correlation between asymmetry in the low-latitude ground perturbation and the dawnside high-latitude ground perturbation. We further show that these periods are characterized by the penetration of mesoscale bursty bulk flows (BBFs) into the dawnside inner magnetosphere. In the context of this event we find that the development of the asymmetric ring current, which inflates the dusk-side magnetotail, leads to asymmetric reconnection and dawnward-biased flow bursts. This results in an eastward expansion and multiscale enhancement of the dawnside electrojet. The electrojet enhancement extends across the dawn quadrant with localized enhancements associated with the wedgelet current systems of the penetrating BBFs. Finally, we connect this work with recent studies that have shown rapid, localized ground variability on the dawnside which can lead to hazardous geomagnetically induced currents.

Plain Language Summary

During geomagnetic storms, electric currents in space can have a dramatic effect on the magnetic field on the ground, causing so-called geomagnetic disturbances (GMDs). Storm-time GMDs exhibit a lopsided asymmetry: dusk-biased near the equator and dawn-biased at high latitudes where aurora usually occur. This asymmetry has been interpreted as a giant wedge-like current system, a dawnside current wedge (DCW). Using a high-resolution supercomputer model, we successfully reproduced the DCW and showed that it occurred during a period of intense, localized flow bursts, akin to bubbles, on the nightside of near-Earth space. The bubbles' buoyancy propels them from the nightside inwards toward dawn, driving intense currents into the Earth's atmosphere. Our simulations suggest that the causal agent of these dawnside bubbles is magnetic reconnection, typically symmetric but skewed dawnward due to asymmetry in the ring current, a crescent-shaped population of energetic ions in space which intensifies during geomagnetic storms. Understanding the cause of stormtime GMD asymmetry is not only important to characterize how electric currents bind the magnetosphere and upper atmosphere, but also to mitigate space weather hazards, as intense GMDs can disrupt and damage power systems on Earth.

1 Introduction

A defining feature of geomagnetic storms is the depression of the geomagnetic field at sub-auroral, i.e. low- and mid-latitudes (Sugiura, 1961). During the main phase of storms, the magnitude of these depressions have long been known to exhibit substantial asymmetry in magnetic local time (MLT), with larger depression at dusk than dawn, while during the recovery phase the depressions are largely MLT-symmetric (Sugiura, 1961). The ground dawn-dusk asymmetry has traditionally been interpreted as a consequence of the longitudinal reduction of a portion of the westward-flowing ring current, called the partial ring current (PRC) as distinct from the symmetric ring current (e.g., Fejer, 1961; Fukushima & Kamide, 1973; Roelof, 1989). Fukushima and Kamide (1973) modeled the PRC as a wire current with a portion of the ring current diverted into the ionosphere in the post-noon sector, flowing eastward within the duskside auroral electrojet (AEJ), and closing through field-aligned currents into the nightside magnetosphere. Within this interpretation the dawn-dusk asymmetry of the ground depression is the combined effect of both the enhanced intensity of the duskside ring current and the duskside depression within the interior of Region 2 (R2) sense field-aligned current (FAC) pair.

That there is, during storm main phase, a ring current that is 'partial', referring to the longitudinal asymmetry of the westward current, has been well established from ENA imaging (e.g., Roelof, 1989; Roelof et al., 2004) and in situ measurements (e.g., Korth et al., 2000; Ebihara et al., 2002). However, the question of how this current closes has not yet been established. Early work focused on the ionospheric closure (e.g., Fukushima & Kamide, 1973; Roelof, 1989), but later work has also emphasized the non-negligible role of the eastward 'banana' current that must flow in the magnetospheric equator on the earthward-edge of the ring current pressure peak (Sitnov et al., 2008; Liemohn et al., 2013; Stephens et al., 2016). Finally, some portion of the current may flow into the duskside and post-noon magnetopause current system (Sitnov et al., 2008).

More recently, Ohtani (2021) conducted a statistical study utilizing SuperMAG (Gjerloev, 2012) ground magnetometer data spanning ~ 700 storms to test the original PRC interpretation, in which ionospheric current closure through the duskside AEJ is a core component. To this end, they used the SuperMAG ring current (Newell & Gjerloev, 2012) and auroral (Newell & Gjerloev, 2014) indices, to demonstrate that dawn-dusk asymmetry in the ring current index is only weakly correlated with enhancement of the duskside eastward AEJ. Instead they find that dawn-dusk asymmetry in the ring current index is strongly correlated with enhancement of the *dawnside* westward AEJ. This led them to propose, as an alternative to duskside AEJ closure, a dawnside current wedge (DCW) model consisting of a Region 1 (R1) sense FAC pair entering the ionosphere prenoon and exiting post-midnight with ionospheric current closure through the dawnside AEJ. In effect, the DCW is morphologically similar to a substorm current wedge (SCW; see Kepko et al., 2015)) but shifted dawnward. The statistical study of Ohtani (2021) built on previous work which found that during major storms the dawnside AEJ often enhances at postmidnight and then extends eastward (Ohtani et al., 2018). Taken together, these results show that the DCW is a persistent and recurrent phenomena during storm main phase and therefore a fundamental aspect of magnetosphere-ionosphere (MI) coupling during geomagnetic storms.

Understanding the closure of magnetospheric currents through the ionosphere during stormtime is crucial to explain the dawn-dusk asymmetry of stormtime geomagnetic disturbances (GMDs). Beyond this, building that understanding has practical implications on human society and infrastructure. Fluctuations in the ground magnetic field caused by GMDs induce a geoelectric field (GEF) in the conducting Earth which can lead to geomagnetically induced currents (GICs), which can damage and disrupt power systems (see Pulkkinen et al., 2017, and references therein). As our understanding of hazardous GMDs has evolved, increasing attention has been devoted to the role of spatially localized effects (e.g., Pulkkinen, 2015; Ngwira et al., 2015) and rapid temporal variation, i.e. large dB/dt (e.g., Pulkkinen et al., 2011; Kataoka & Ngwira, 2016; Engebretson, Pilipenko, et al., 2019), in creating hazardous space weather. Additionally, recent work has highlighted the importance of understanding dawnside/morning currents during stormtime as a space weather concern (Ohtani et al., 2018; Apatenkov et al., 2020; Schillings et al., 2022; Milan et al., 2023). In particular, statistical studies of the MLT distribution of large dB/dt spikes have shown a hotspot in the dawnside/morning sector (Schillings et al., 2022; Milan et al., 2023) and these spikes have been connected to dawnside auroral Omega bands (Schillings et al., 2022; Zou et al., 2022), a particular kind of mesoscale auroral form exhibiting undulations on the poleward edge of the auroral oval (see Forsyth et al., 2020, and references therein). Finally, a report by the Electric Power Research Institute (EPRI; EPRI, 2020) found that localized (~ 200 km) GEF enhancements had the highest rate of occurrence in the pre-dawn (0300-0600 MLT) sector and that these localized enhancements can have adverse effects on power systems beyond the enhancement itself.

Turning now to this work, our intention is to investigate the DCW using global modeling. Specificaly, we first show that global geospace modeling can reproduce this ubiquitous stormtime feature and then use the model to identify the underlying causal processes, and their spatial scales, that lead to it. We note that here DCW refers to both the stormtime *phenomenon*, namely the correlation between dawn-dusk ring current asymmetry and dawnside auroral enhancement, and the *interpretation* of this phenomenon by Ohtani (2021) as a wedge current system. To this end we take as a case study, the well-documented March 2013 "St. Patrick's Day" geomagnetic storm and model this event using the Multiscale Atmosphere-Geospace Environment (MAGE) model (K. A. Sorathia et al., 2020; Lin et al., 2021; Pham et al., 2022). The MAGE model has previously been used to study the role of mesoscale processes in magnetosphere-ionosphere (MI) coupling (Lin et al., 2021; K. A. Sorathia et al., 2020) and dawnside phenomena during stormtime, specifically dawnside subauroral polarization streams (Lin et al., 2022).

The presentation of our results in the remainder of the paper is organized as follows. Section 2.1 describes the details of our simulation of the chosen event, a well-studied, moderate geomagnetic storm. We provide an overview of the SuperMAG geomagnetic indices, and how we calculate 'synthetic', meaning derived from model data, indices in Section 2.2. In Section 2.3 we show data-model comparisons of the SuperMAG indices, with MLT granularity, throughout the modeled event.

Our main results are presented in Section 3 wherein we focus our attention to a period of several hours during which we find an instance of a DCW. We show that the model reproduces the phenomenology of the DCW (Section 3.1) and that the DCW in the model is connected to the penetration of dipolarizing, mesoscale flows into the dawnside inner magnetosphere (Section 3.2). We then show contemporaneous observational data supporting the role of dawnside mesoscale flow bursts (Section 3.3). Concluding our main results, we present an analysis of global geospace current closure and the current budget governing the dawnside AEJ enhancement (Section 3.4). This is followed by a brief discussion interpreting our results in the context of stormtime geospace processes and the implications of our results for understanding GIC hazards (Section 4). Finally, we conclude with a brief summary of our results (Section 5).

2 Methodology

2.1 Simulation

For our investigation into the DCW we use as a case study the March 2013 "St. Patrtick's Day" geomagnetic storm, a relatively modest storm for which there exists robust in situ data and a substantial body of existing literature. We simulate the storm using the MAGE model (K. A. Sorathia et al., 2020; Lin et al., 2021, 2022; Pham et al., 2022). In the model configuration we use here, MAGE includes the global MHD model GAMERA (Zhang et al., 2019; K. A. Sorathia et al., 2020), the inner magnetosphere model RCM (Toffoletto et al., 2003), and the ionospheric potential solver REMIX (Merkin & Lyon, 2010). While each model has its own resolution and grid, which we discuss further below, we can take as a fiducial resolution estimate 600 km in the central plasma sheet and $0.5°$ in the ionosphere. In the remainder of this section we provide information about the configuration, resolution, and coupling mechanisms used. These details are broadly similar to those used in other applications of the MAGE model.

Like LFM (Lyon et al., 2004), the GAMERA MHD grid is a warped spherical grid with: axis aligned with the Solar Magnetic (SM) X-direction; dayside extent 30 R_E; tailward extent 300 R_E; dawn-dusk symmetry with extent along the terminator 100 R_E; and spherical inner boundary located at 1.5 R_E. The grid used here, termed "OCT", uses $192 \times 192 \times 256$ grid cells in the radial, azimuthal, and polar directions. The distorted nature of the grid allows the flexibility to concentrate cells in regions of interest while smoothly transitioning to coarser regions. The "OCT" grid is $2\times$ coarser than the "HEX" grid used in K. A. Sorathia et al. (2020), which reached ion kinetic scales in the plasma sheet.

The inner boundary condition of the MHD simulation, at $R = 1.5\ R_E$, enforces zero-gradient conditions on the plasma density and pressure and for the velocity, $V_r = 0$ with the transverse components defined via an electrostatic potential solution. The electrostatic potential is calculated by enforcing current closure of the MHD-derived FACs mapped to a thin-shell ionosphere at $\approx$ 120 km altitude along with a specification of the height-integrated conductance (Merkin & Lyon, 2010). In the simulation presented here, the electrostatic potential is calculated on an ionospheric grid of $0.5^\circ \times 0.5^\circ$ resolution with equatorward boundary set by the dipole mapping of the MHD inner boundary radius ($1.5 R_E$) and solved at a cadence of 5 seconds.

The height-integrated conductance is specified from a precipitation model using the Robinson formulas (Robinson et al., 1987), with the correction described by Kaeppler et al. (2015). The electron precipitation model is described in detail by Lin et al. (2021), but we provide a brief overview here. MAGE uses a precipitation model that separately accounts for mono-energetic and diffuse electron precipitation. The mono-energetic precipitation is derived from the MHD density, temperature and FAC on the inner boundary of the MHD simulation and is only present in regions of upward FAC. Diffuse precipitation is informed in the inner magnetosphere by the energy-dependent losses applied to each energy channel of the RCM, which we describe below. In this way, we are able to capture eastward-propagating conductance enhancements due to localized energetic electron injections.

Coupling to the inner magnetosphere model, RCM, is done in a manner that is broadly similar to Pembroke et al. (2012) with various improvements. In particular, we do not limit the coupling domain based on flow speed or plasma β, to allow the coupling domain to better capture the ring current pressure peak during the main phase of a storm. Instead we fit an ellipse within the closed field region of the equatorial magnetosphere, based on the changing MHD field lines, along with the constraint that the equatorial magnetic field strength be larger than 1 nT. This is followed by several iterations of smoothing of the boundary on the RCM's ionospheric latitude-longitude grid. The spatial domain of the RCM grid has a resolution of $0.25^\circ \times 1^\circ$ in latitude and longitude, respectively. The RCM evolves the bounce-averaged, isotropic drift kinetic equations (Wolf, 1983) by discretizing a plasma distribution function over a series of channels, defined via an energy invariant. In this work, we use 115 energy channels: 29 channels for electrons, with peak energy corresponding to $\approx$ 10 keV at geosynchronous; 85 channels for protons, with peak energy corresponding to $\approx$ 100 keV at geosynchronous; and a single zero-energy channel to represent a cold plasmasphere.

The RCM coupling is done at a cadence of 10 seconds, with updated plasma density and pressure being ingested into the MHD solution with a characteristic timescale defined by the transit time of an Alfven wave along the local field line. Electron losses are calculated using a simple approximation of 1/3 the strong scattering rate, while ion losses are calculated using the estimated charge exchange loss rate based on the energy-dependent charge exchange cross-section (Lindsay & Stebbings, 2005) and an assumed geocorona density profile (Østgaard et al., 2003). The ions and electrons are initialized based on a combination of a plasma sheet and quiet-time ring current. The plasma sheet is specified by the empirical relationship of Borovsky et al. (1998). The quiet-time ring current is specified by an axisymmetric profile as in Liemohn (2003) whose total energy density is constrained by the D_{ST} at the start of the event and the relationship between D_{ST} and energy density given by Dessler and Parker (1959). The plasmasphere is initialized based on the Kp-dependent empirical model of Gallagher et al. (2000). After initialization, boundary conditions are provided to RCM using MHD-derived flux tube-averaged density and pressure mapped to the RCM energy invariant grid and assuming a constant electron-ion temperature ratio. Sciola et al. (2023) recently presented a detailed data-model comparison for this event using the MAGE model, with a specific focus on the buildup of the ring current and its energy-dependent intensity.

After a period of preconditioning the simulation is run starting from 00:00 UT on 17-3-2013 (day-month-year) for a period of 30 hours. The solar wind boundary condition is derived from NASA's OMNIWeb 1-minute cadence data, with gaps in the data filled using linear interpolation. The solar wind conditions for the event are shown in Figure S2. Full model output was saved at a cadence of 30-seconds. Dataset S1 contains the full model output during the 1-hour period, 10:00-11:00 UT on 17-3-2013, at reduced cadence, 5 minute, that is the main focus of our investigation. Dataset S1 along with its contents and format are described in further detail in the Supplementary Information.

2.2 Diagnostics

Throughout much of our analysis in this work we will make use of the indices introduced by SuperMAG (Gjerloev, 2012; Newell & Gjerloev, 2012, 2014). In particular SMR, SMU, and SML which are analogous to SYMH, AU, and AL respectively. While these are described in detail elsewhere, for convenience we will briefly summarize them here and discuss how we calculate synthetic indices from the model data. In what follows we will use ΔB_N to refer to the ground magnetic perturbation in the direction of magnetic north and λ_M to denote the magnetic latitude of the measurement. The auroral indices, SML and SMU, are defined as the minimum and maximum, respectively, of ΔB_N taken over the available ground measurements for which $40^\circ < \lambda_M < 80^\circ$. The real power of the SuperMAG indices, however, is MLT granularity. For SML, and analogously for SMU, there are 24 indices spanning MLT, SML-LT, which are defined similarly to SML but taken over sliding 3 hour MLT windows. For instance, $SML12$ is centered at 12:30 MLT and uses the MLT window spanning 11:00-14:00. To calculate the SMR index, the first step is calculating the average of $\Delta B_N / \cos(\lambda_M)$ for $|\lambda_M| < 50^\circ$ over equally sized local time quadrants centered at midnight, dawn, noon, and dusk to construct $SMR00$, $SMR06$, $SMR12$, and $SMR18$ respectively. The global SMR is then defined as the arithmetic average of these quadrant-based SMR-LTs..

To calculate synthetic SuperMAG indices from the model data we must calculate the ground magnetic disturbance, ΔB. To do this we follow the approach of Rastätter et al. (2014), effectively the Biot-Savart integral over the external currents in the model: J_{MAG}, the magnetospheric currents from the MHD simulation; J_{ION}, the height-integrated ionospheric currents including both Hall and Pederson, from the ionospheric electrostatic solver; and finally J_{FAC}, the field-aligned currents in the volume bounded by the spherical inner boundary of the MHD simulation, at $R = 1.5\ R_E$, and the spherical shell where the horizontal currents of the ionosphere are calculated, $R \approx 1.02\,R_E$. In this manner we calculate ΔB on a $0.5^\circ \times 0.5^\circ$ spherical grid on the surface of the Earth. Synthetic indices are calculated based on ΔB_N, where the definition of magnetic north and magnetic latitude assumes a centered dipole aligned with the SM-Z axis.

When calculating synthetic indices based on model data we have the option to either use virtual stations based on the locations of the available SuperMAG stations, or to approximate full ground coverage using the entire densely populated grid we calculate ΔB on. Figure 1 shows a comparison of the synthetic SMR calculated in both ways along with the SuperMAG SMR. For convenience, Figure 1 also includes selected solar wind drivers from the full solar wind conditions depicted in Figure S2. While there are some isolated discrepancies between the synthetic indices, due to limitations of station coverage, we find them to be fairly minor. Figure 2 shows a similar comparison of SMU-LT and SML-LT, which shows more noticeable differences between synthetic indices when

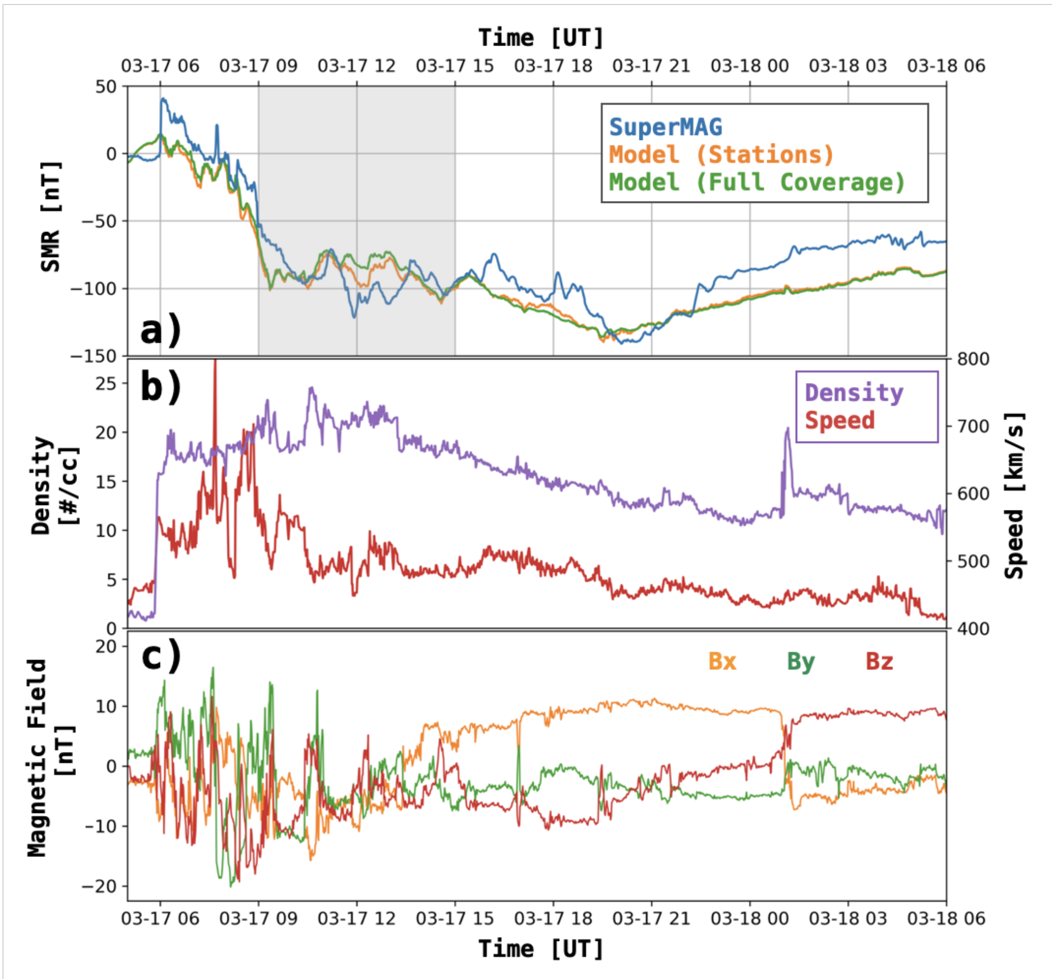

Figure 1. Data-model comparison of *SMR* and key solar wind drivers. Comparison of the SuperMAG *SMR* index, analogous to SymH, with synthetic indices calculated from the simulation (a). Synthetic indices are calculated in two ways: using only synthetic measurements at SuperMAG station locations (Stations), and by using all points on a dense ground grid (Full Coverage). Also shown are solar wind density (b; left axis) and speed (b; right axis), as well as IMF components (c). Full solar wind conditions are shown in Figure S2.

using virtual stations as opposed to full coverage. For instance, there are eastward-propagating features in *SMU*-LT (Figures 2a and 2c) that do not appear in the full coverage calculation (c.f. Figures 2c and 2e), as they are caused by a sparse coverage region and its rotation. In most of the analysis that follows we will, when using synthetic SuperMAG indices, use the measurements of ΔB_N on the full $0.5^\circ \times 0.5^\circ$ ground grid.

2.3 Data-Model Comparison of SuperMAG Indices

Before moving on to our main scientific results, we present here a data-model comparison of the SuperMAG geomagnetic indices for the event we are studying. In particular, we show that the model is able to reproduce the overall stormtime phenomenology as measured by ground magnetometers and also the dawn-dusk asymmetries critical to the phenomenology of the DCW as identified by Ohtani (2021).

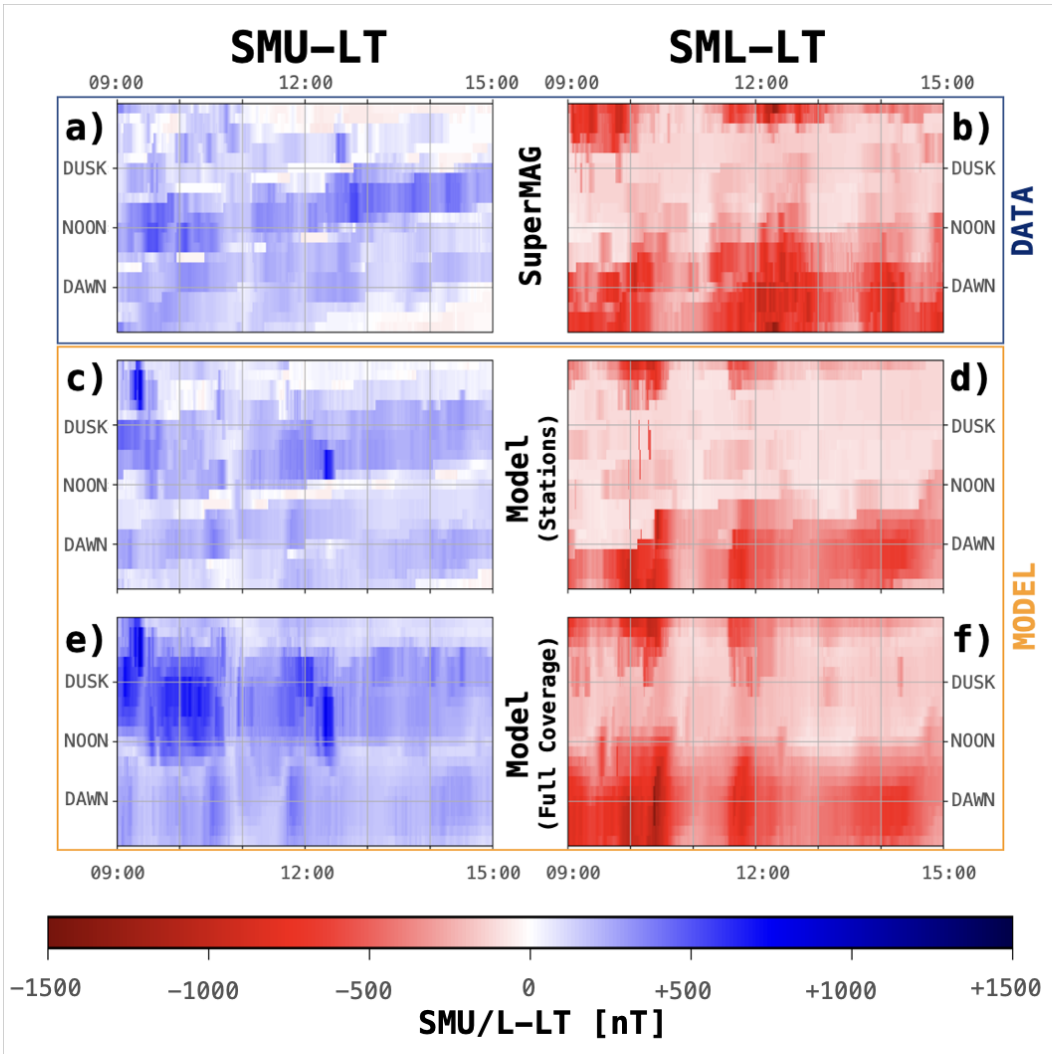

Figure 2. Data-model comparison of *SML*-LT and *SMU*-LT. Comparison of SuperMAG auroral indices, upper (a) and lower (b), with MLT granularity to synthetic indices calculated from the simulation. Synthetic indices are calculated using either: only measurements at interpolated SuperMAG station locations (Stations; c and d), or by using all points on a dense ground grid (Full Coverage; e and f). Time interval shown corresponds to the early main phase, the shaded region in Figure 1a.

We begin with a comparison of *SMR*, the SuperMAG analog to SYMH, shown in Figure 1. In the comparison of *SMR*, we see in both the data and the model a two-stage drop in the *SMR*, to −100 nT and subsequently to −140 nT, and an approximately linear recovery beginning at 21:00 UT. We note there is an early discrepancy at the storm sudden commencement (SSC), which is primarily due to linearly interpolating gaps in the OMNI solar wind data used to drive the simulation (Figure S2). We also note that the model does not perfectly reproduce the two-timescale recovery phase, likely a limitation of how ring current loss processes are modeled. As described in Section 2.1, ring current ion losses are treated using an empirical geocorona model and the energy-dependent charge exchange cross-section. Ilie et al. (2013) showed that the recovery timescales vary substantially based on different choices of empirical geocorona model. Even if the true geocorona profile was known, small inaccuracies in the modeled ring current, in the radial and/or energy profile, will be magnified in the predicted recovery due to the steep radial profile of geocorona density and energy-sensitivity of the charge exchange cross section. However, despite these caveats we do accurately reproduce the observed *SMR* over the course of the storm. In the remainder of this work we focus on the early main phase of this storm, the shaded region in Figure 1a, to investigate the DCW.

Next we turn to a comparison of the auroral indices, with MLT granularity, *SML*-LT and *SMU*-LT shown in Figure 2. In Figure 2 the left and right columns are *SMU*-LT and *SML*-LT, respectively, and the rows, from top to bottom, are: the official SuperMAG indices; the synthetic indices derived from the model using only the virtual station locations; and the synthetic indices derived from the model assuming full ground coverage. The eastward propagating features in SMU-LT due to station coverage were discussed in Section 2.2 and here we will focus on the features in SML-LT that will be most relevant to the DCW.

Comparing the dawnside *SML*-LT, in both data and model (Figure 2b and d) we find: periods of activation and eastward expansion of the dawnside AEJ, e.g. between 9:45 and 10:30 UT; alternating with periods of relative dawnside quiescence, e.g. between 10:30 and 11:15. In this overall morphology the data and model are in qualitative agreement, however we do note that there are quantitative discrepancies. Specifically, the model overpredicts the dawnside AEJ enhancement around 10:15 while it underpredicts the magnitude and duration of the AEJ enhancement seen in the data around 12:00. In the data we find a shorter, weaker dawnside AEJ enhancement followed by a period of quiescence and then a longer, stronger dawnside AEJ enhancement whereas this sequence is reversed in the model. This reversed sequence can also be seen in Figure S3 which shows *SML* and *SMU* in the manner of Figure 1a. In the first AEJ enhancement we find *SML* to be approximately −1250 nT and −1000 nT in the model and data, respectively, with quiescent values of approximately −300 nT in both, followed by a second AEJ enhancement with *SML* reaching approximately −750 nT and −1250 nT in the model and data, respectively. In total, we find that the model reproduces the on-off-on sequence in the dawnside AEJ and its eastward expansion, and the model reproduces the minimum *SML* during this period, albeit offset in time.

Lastly, we return to the low-latitude equatorial depression as encapsulated by *SMR*, focusing on the dawn-dusk asymmetry shown by comparing *SMR*06 versus *SMR*18. To this end we define,

$$\Delta SMR06 \triangleq SMR06 - SMR, \tag{1}$$

with similar definitions for the other MLT quadrants, and

$$\Delta^{06}_{18} SMR \triangleq \Delta SMR06 - \Delta SMR18. \tag{2}$$

Figure 3 shows *SMR*06 and *SMR*18 from SuperMAG and the synthetic analog from the model, using the full coverage assumption. Here we find that the quantitative agree-

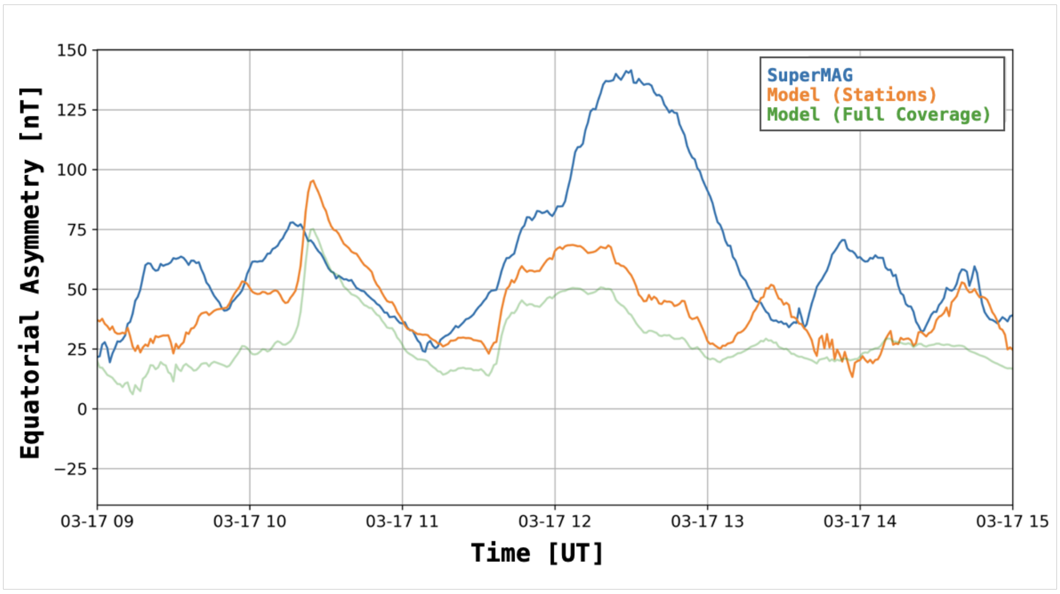

Figure 3. Data-model comparison of dawn-dusk SMR asymmetry. Shown is the difference between dawn and dusk SMR, $\Delta_{18}^{06}SMR$ (Equation 2). Synthetic indices are calculated in two ways: using only synthetic measurements at SuperMAG station locations (Stations), and by using all points on a dense ground grid (Full Coverage).

ment is less striking than in the MLT-averaged SMR comparison, c.f. Figures 1 and 3, but the model does reproduce the core qualitative features of the interval. In particular, Figure 3 shows that in the early main phase there are periods of dawn-dusk asymmetry in SMR followed by intervals of near-symmetry, i.e. local minima of $\Delta_{18}^{06}SMR$. Similar to the dawnside AEJ enhancement, we find an on-off-on sequence. At approximately 10:30 UT both the data and model show $\Delta_{18}^{06}SMR \approx 75$ nT, which decreases to $\Delta_{18}^{06}SMR \approx$ 25 nT at 11:15 UT and then rises again between 11:30 and 12:00 UT. Also similar to the dawnside AEJ enhancement, the model underpredicts the magnitude and duration of the second peak.

In summary, we have shown that the model adequately reproduces for this event the global system evolution in the most typical stormtime index, SMR (Figure 1a); the temporal and MLT evolution of the auroral indices (Figures 2 and S3); and finally, the onset times, intervals, and approximate magnitudes of the periods of dawn-dusk asymmetry in SMR (Figure 3). The former is simply a typical data-model comparison, while the latter two are more discerning metrics that provide us confidence that we can use the model to diagnose the underlying physics at play during the DCW.

3 Results

3.1 Validating DCW Phenomenology in the Model

The core phenomenology of the DCW as identified by Ohtani (2021) is the anticorrelation between dawn-dusk asymmetry in the low/mid-latitude stormtime perturbation, proxied by $SMR06 - SMR18$, and the enhancement of the dawnside westward electrojet, proxied by $SML06$, as opposed to the duskside eastward electrojet, proxied by $SMU18$. Using the synthetic indices calculated from the model data, as described in Section 2.2, we can verify that the model reproduces these relationships.

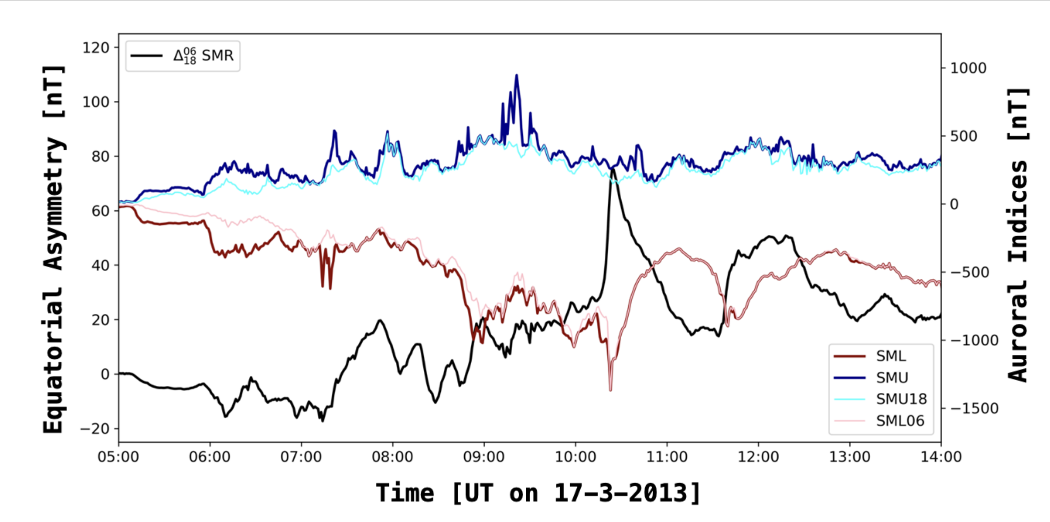

Figure 4. Phenomenology of the dawnside current wedge. Comparison of the dawn-dusk SMR asymmetry, $\Delta^{06}_{18}SMR$ (Equation 2; left axis), to auroral indices (right axis). All indices shown are calculated from the model using 'Full Coverage' ground measurements.

The correlation between equatorial asymmetry and auroral indices is shown in Figure 4. From this it can be seen that in the model there are peaks in $\Delta^{06}_{18}SMR$ at approximately 10:30 and 12:15 that last for approximately 1 hr and correspond to $\approx 50-100$ nT dawn-dusk asymmetry. During both periods of equatorial asymmetry, there are clearly correlated dips in SML and that these dips are driven by the dawnside behavior, c.f. $SML06$ and SML. Conversely, there is negligible correlation between the equatorial asymmetry and the duskside electrojet response, c.f. $\Delta^{06}_{18}SMR$ and $SMU18$. This shows that the model reproduces the phenomenology of the DCW as manifested on the ground.

Expanding upon Figure 4, Figure S4 shows $\Delta^{06}_{18}SMR$ against SML at local times spanning MLT. From this we find that the strongest correlations with $\Delta^{06}_{18}SMR$ occur between $SML03$ to $SML09$, the full dawn quadrant, with weaker correlation spanning $SML00$ to $SML12$. The MLT extent and evolution of the dawnside electrojet can be seen, in both the model and data, in Figure 2. There we see both the enhancement of the dawnside electrojet and its eastward expansion, eventually reaching noon.

3.2 Investigating the Modeled DCW

Next, we can turn our attention from validation to investigation and use the model to explore the geospace processes that occur during stormtime that give rise to the DCW and whether it is indeed a current wedge. As a starting point, we pick the period at 10:30 which shows the strongest DCW behavior (Figure 4) and consider the geospace configuration at this time.

To provide an overview of the geospace configuration during the DCW, Figure 5 shows a 'simulation at a glance' plot taken at approximately 10:30UT, during the early main phase of the storm. The overview plot shows: equatorial ΔB_Z (left panel); equatorial pressure from the inner magnetosphere model (left panel inset); meridional pressure (right panel); and ionospheric FACs in the northern and southern hemisphere (top and bottom insets of right panel, respectively), oriented such that noon and dawn are right and down, respectively. An animated version of Figure 5 is available in Movie S1. Seen in the overview plot, and its evolution in Movie S1, is the penetration of dipolar-

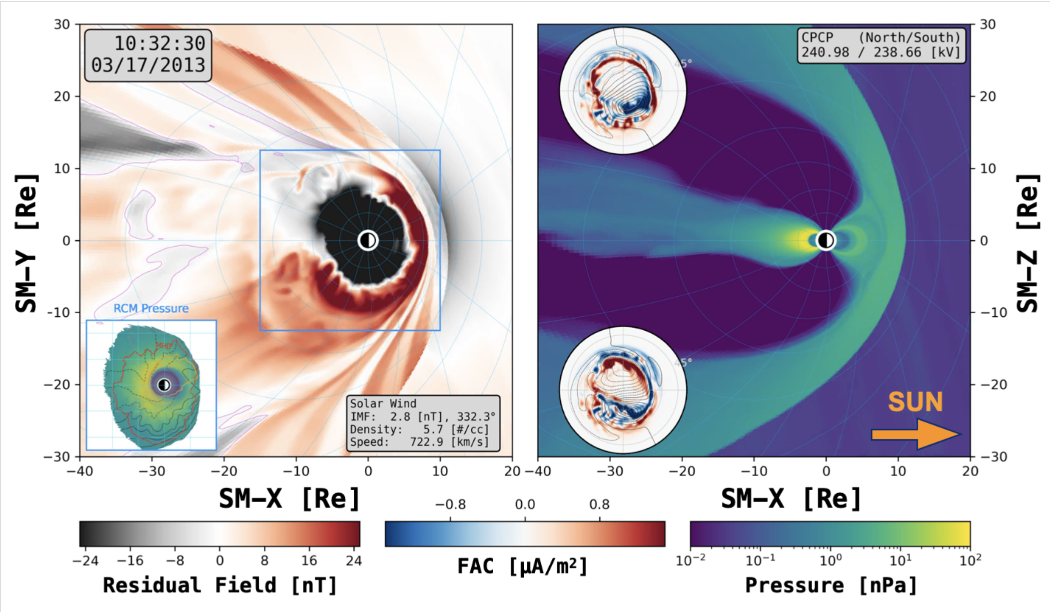

Figure 5. Simulation at a glance. Snapshot of the simulation during the fiducial DCW. Shown are the equatorial residual, i.e. non-dipolar, magnetic field (left panel) and the equatorial ring current pressure from the inner magnetosphere model (left panel, inset). Also shown are the meridional pressure (right panel) and the FACs in the northern and southern ionosphere (right panel, insets). All plots are consistent in orientation in that the Sun is to the right. Movie S1 contains an animated version of this plot.

izing, mesoscale flows into the dawnside inner magnetosphere. The effect of these flows can be seen in the complex FACs in the dawnside R2 current. Figure S5 shows the state of the inner magnetosphere at approximately the same time as Figure 5 and demonstrates that these intruding flows are associated with depleted flux-tube entropy 'bubbles' (Pontius Jr. & Wolf, 1990). These flows originate in the near-Earth plasma sheet (Movie S1) as bursty bulk flows (BBFs; Baumjohann et al., 1990; Angelopoulos et al., 1992). However, as we will primarily be focused on the consequences of these flows in the inner magnetosphere, as opposed to the plasma sheet, we will typically refer to them as bubbles.

To better understand the MI coupling during these DCW intervals, we show in Figure 6 a series of panels to illustrate the connection between flows in the inner magnetosphere and their consequences on the ionosphere. The top panel, Figure 6a, shows the evolution of SMR and each quadrant-based SMR over the early main phase. The remaining panels, Figures 6b through d, are "spacetime" plots which show various quantities calculated in the magnetospheric equator at $R = 6R_E$ and plotted as functions of MLT, excising the quadrant centered at noon, and UT, i.e. for a quantity Q

$$Q(R = 6R_E, \mathrm{UT}, \mathrm{MLT}). \quad (3)$$

For Figures 6b through d, respectively, the choice of Q is: ΔB_Z, the non-dipolar compnent of the northward magnetic field; $j_{\|}^{V}$, the FAC calculated using the Vasyliunas equation (Vasyliunas, 1970); and finally, the precipitating electron energy flux into the ionosphere which is used to inform the ionospheric conductance in the model (see Section 2.1). Figure S6 is identical to Figure 6 with the time range focused on the periods of peak $\Delta_{18}^{06}SMR$. The use of the Vasyliunas equation allows us to easily calculate the inner magnetospheric FACs at the $R = 6R_E$ arc, but requires certain assumptions like the negligible contribution of inertial terms. In Section 3.4 we will show, by tracing the magnetic field backwards from the ionosphere, that the assumptions of the Vasyliunas equation do not affect the behavior we identify here.

Figure 6 illustrates that subsequent to both peaks in $\Delta^{06}_{18}SMR$, occurring at 10:30UT and 11:45UT, there are broad dipolarizations across all MLT with localized, dipolarizing flows on the dawnside. In particular, we note the similarity between the localized, dipolarizing flows on the duskside early in the storm (Figure 6b, 7:30UT) and the later dawnside penetrating flows. Turning now to the FACs, Figure 6c shows currents from the equator into the ionosphere as red and the reverse as blue, MLT centered at midnight with the vertical direction corresponding to westward. With this orientation, red vertically above blue corresponds to R2 polarity. An undisturbed, wide R2-sense current system can be seen prior to 7:30UT and this system largely remains as a background throughout the time interval shown. This can be interpreted as the result of the pressure buildup of the ring current during the main phase of the storm. Next, we find that during the early period when duskside bubbles penetrate into the inner magnetosphere that there are a series of R1-sense "wedgelets" (Rostoker, 2013; Liu et al., 2013) coincident with the individual flow structures. We find similar R1-sense wedgelets during the later periods of enhanced $\Delta^{06}_{18}SMR$ and *SML* (Figure 4) and dipolarizing bubbles inside of geosynchronous (Figure 6b).

Figure S7 shows a snapshot from the simulation at illustrating the connection between dipolarizing bubbles and R1-sense wedgelets. It shows the colocation of the localized, dipolarizing flows and R1-sense FACs mapped to the magnetospheric equator from the ionosphere, without relying on the assumptions of the Vasyliunas equation. Returning to Figure 6c, we note that the evolution of these wedgelets trend westward consistent with the energy-dependent drifts of energetic ions. Finally, we turn to the precipitating energy flux (Figure 6d). Here we find that during the DCW periods there are localized precipitation enhancements and that they drift eastwards, consistent with energetic electron drifts.

In summary, we have found that periods of dawn-dusk asymmetry in *SMR* are coincident with the penetration of azimuthally localized, dipolarizing flows into the dawnside inner magnetosphere followed by broader MLT-wide dipolarization. The localized, dipolarizing flows are colocated with pressure-generated R1-sense wedgelets and localized regions of enhanced precipitation which subsequently drift eastward. Figure S5 shows that these penetrating flows are associated with depleted flux-tube entropy and enhanced temperatures. Therefore, we interpret the model as showing that the DCW periods are characterized by the dawnside penetration of dipolarizing bubbles which lead to energetic particle enhancements in the inner magnetosphere.

3.3 Observations During the DCW

Our initial investigation of the modeled DCW (Section 3.2) highlighted the role of dipolarizing, dawnside, mesoscale magnetospheric flows. With these insights in mind, we now show that the model results are supported by contemporaneous data during this interval. Specifically, we will show: SuperMAG (Gjerloev, 2012) and GOES (Singer et al., 1996) data that supports dawnside, eastward-propagating dipolarization; and TWINS (McComas et al., 2009) and AMPERE (Waters et al., 2020) data which supports flow bursts penetrating into the dawnside inner magnetosphere.

The evolution of the dawnside auroral electrojet can be inferred from the SuperMAG *SML* indices. Figure 7 is similar to Figure 2b but focused on the time interval we have investigated in the model (e.g., Figure 6). Additionally, we have added markers on the SuperMAG *SML*-LT index to show at each UT which ground station measures the strongest negative ΔB_N deflection, with the location of the marker designating the MLT of the station and the color of the marker designating its magnetic latitude. The Super-

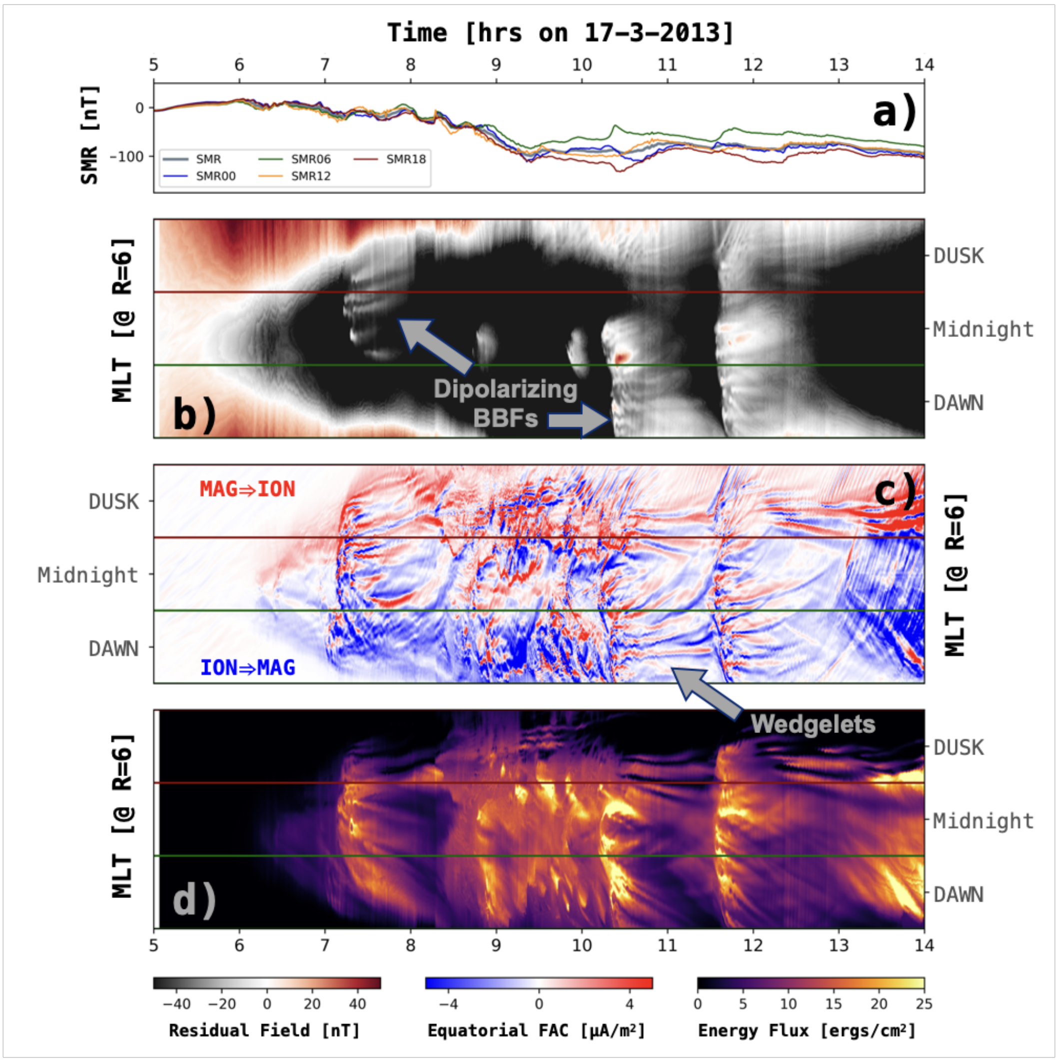

Figure 6. Role of the dawnside inner magnetosphere during the DCW. Shown are the model-derived *SMR* and its constituent quadrants (a), and spacetime plots (b-d), functions of UT and MLT (with noon quadrant excised), taken at $R = 6\ R_E$ in the magnetospheric equator. Spacetime plots show: residual, i.e. non-dipolar, northward magnetic field (b); predicted FAC calculated using the Vasyliunas equation (c); and the precipitating electron energy flux which is used to inform ionospheric conductance (d). Figure S5 shows just the period between 10:00 and 11:00 UT.

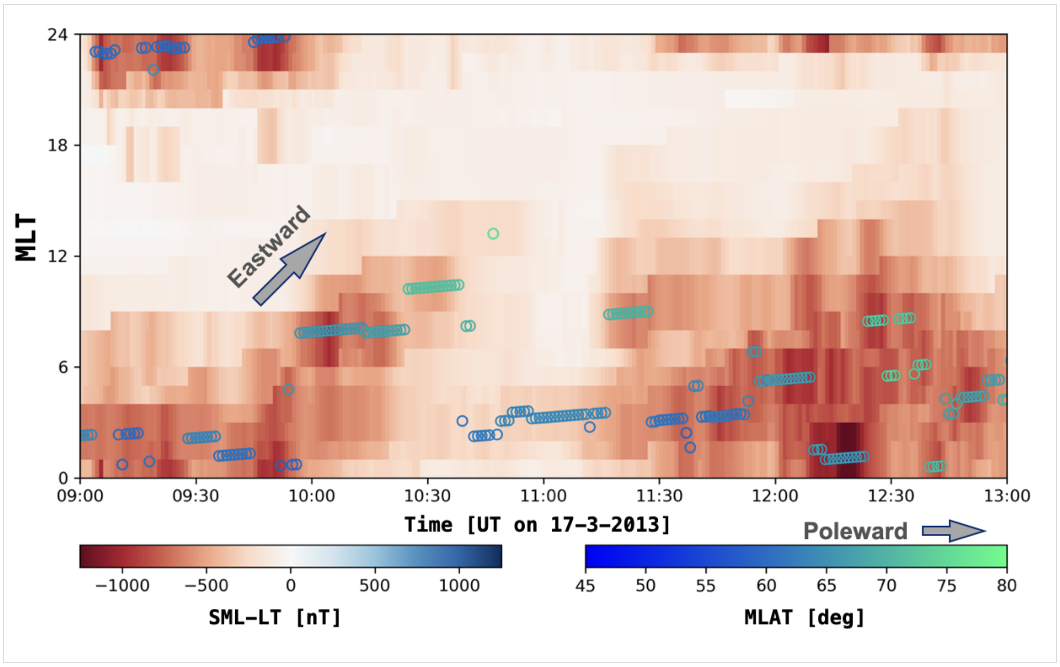

Figure 7. SuperMAG measurements during the DCW. Figure shows real (not model-derived) SuperMAG *SML*-LT index, c.f. Figure 2d, with markers added to denote at each UT the MLT and MLAT of the station measuring the largest negative depression.

MAG data shows two periods characterized by the eastward-expansion of the dawnside AEJ, in both cases reaching noon or further, with an intervening quiescent period. During periods of eastward-expansion of the dawnside AEJ, we also find that the location of minimum ΔB_N moves poleward. Figure S8 shows a similar plot, with magnetic latitude markers for each MLT-hour. Similarly, we find that during this period of eastward-expanding dawnside AEJ, there is a broad poleward shift across the morning sector. Poleward shifts of magnetic footpoints are often considered a signature of dipolarization (Chu et al., 2015), consistent with the dipolarization of the inner magnetosphere we find in the modeled DCW (Figure 6). Additional support for the interpretation of a dawnside dipolarization is provided in Figure S9, which shows GOES data of the northward magnetic field and the model residual magnetic field during this interval. During this interval GOES 13 is near dawn and GOES 15 near midnight. The GOES data shows two periods of dipolarization inside geosynchronous orbit: the first begins shortly after 10:30 and is observed by GOES 13 and not observed by GOES 15, consistent with an eastward-propagating dipolarization starting post-midnight; and a second dipolarization after 11:30 observed first by GOES 15 and subsequently by GOES 13, again consistent with eastward-propagation.

To better understand the relevant spatial scales in the magnetosphere during this period, we consider the plasma sheet ion temperature using ENA reconstruction based on TWINS data (McComas et al., 2009; Keesee et al., 2014). Previous work has used TWINS ENA reconstruction to investigate mesoscale plasma sheet structure (Keesee et al., 2021; Adewuyi et al., 2021) and the data we present here uses the same method. Figures 8a and 8b show the ENA reconstruction during time intervals before and during the peak of the DCW. Most notable is that during the DCW we find 3 distinct, localized temperature enhancements on the dawnside inside of geosynchronous orbit (dashed circle, Figure 8d). The implied evolution between Figures 8a and 8b, the spatial scale of the localized enhancements, and enhanced ion temperature are all consistent with the in-

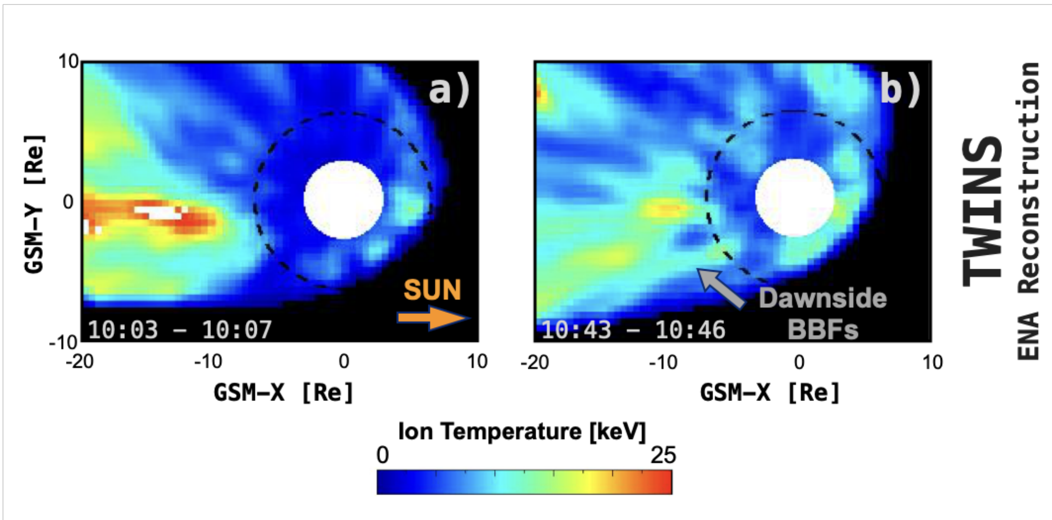

Figure 8. TWINS ENA reconstruction of ion temperature before (left) and during (right) the DCW. AMPERE data at comparable times is shown in Figure S10.

terpretation of these as localized flow bursts penetrating the dawnside inner magnetosphere as we see in the simulation. Moving now to the ionosphere, Figure S10 shows the (Waters et al., 2020) data-assimilated reconstruction of the ionospheric radial current at approximately the same times as shown in Figure 8. The AMPERE data shows a transition from a more typical R1/R2 FAC pattern (Iijima & Potemra, 1976) to one in which there is an apparent disruption in the dawnside R2 current. This suggests either there is an actual absence of the R2 current or that there are near-balanced up-down current pairs below the typical 2.4 hr local time resolution of the AMPERE spherical harmonic fit (Anderson et al., 2014). The latter is consistent with what we see in the modeled ionospheric FACs during the DCW, c.f. Figures S10b and 5 (right-top inset).

In the model we found an eastward-propagating enhancement of the AEJ coincident with the dawnside penetration of dipolarizing mesoscale flows. Here we have shown that all these features are supported by or consistent with contemporaneous observations.

3.4 Geospace Currents During the DCW

Having shown that the key phenomena we have identified in the model are consistent with and supported by contemporaneous measurements, we now return to the model to investigate the evolution and closure of geospace currents during the DCW. To this end we will again use ”spacetime” plots, functions of MLT and time, to connect currents in the equatorial magnetosphere to the dawnside electrojet enhancements.

In the following definitions we make use of magnetic longitude, $\phi = \arctan(Y_{SM}/X_{SM})$, and an indicator function for closed magnetic field lines, $\mathbb{1}_{\mathcal{C}}$, which takes the value 1 if a given point is on a closed magnetic field line, defined as both endpoints of the field line connecting to Earth, and 0 otherwise. Here we define,

$$\mathcal{J}_{EQ}(\phi) = \int_{r<12R_E} -\mathbf{J}_{\perp,\phi}\mathbb{1}_{\mathcal{C}} \cdot r d\theta dr, \tag{4}$$

where r refers to the spherical radius. In other words, we are calculating the cross-field current carried by closed field lines in the near-Earth region, $r < 12R_E$, which we take as a proxy of the ring current and near-Earth portion of the cross-tail current. Defined

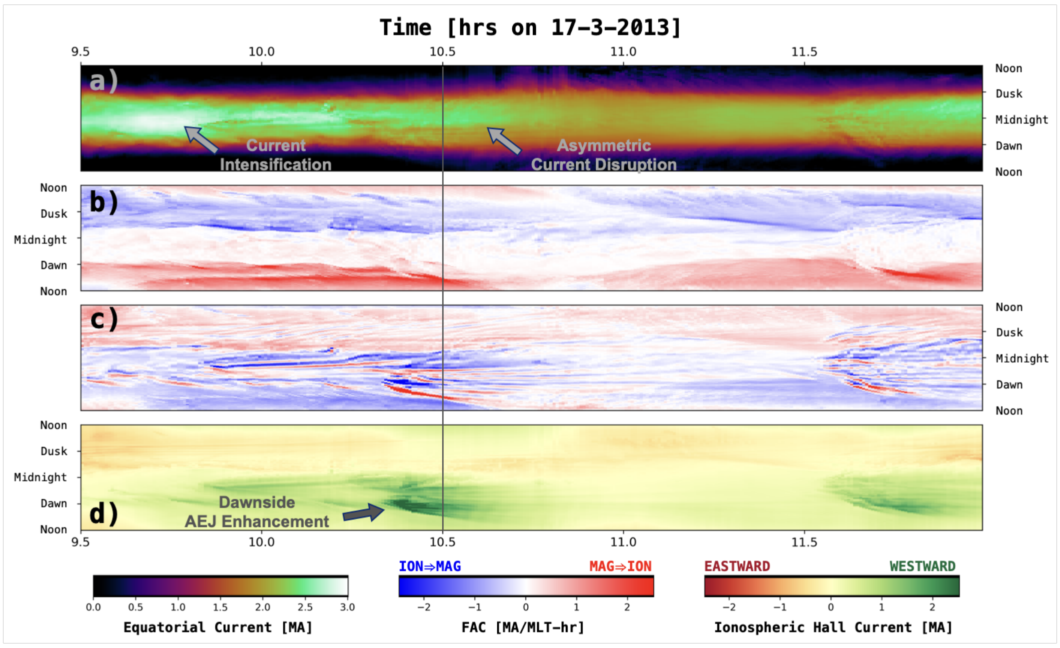

Figure 9. Geospace currents during the DCW. Shown are spacetime plots, functions of UT and MLT, depicting: magnetospheric currents on closed field lines (a); FACs on open field lines (b); FACs on closed field lines (c); ionospheric Hall current (d).

this way, the dawn to dusk cross-tail current and the westward ring current correspond to $\mathcal{J}_{EQ} > 0$. We calculate $\mathcal{J}_{EQ}$ at a longitudinal spacing of 0.5°.

Similarly, within the ionosphere we define

$$\mathcal{J}_{\parallel}^{\mathcal{C}}(\phi) = \int J_{\parallel} \mathbb{1}_{\mathcal{C}} \cdot r^2 \sin(\theta) d\theta, \tag{5}$$

where the integral is taken on the ionospheric grid over all latitudes at the same 0.5° longitudinal spacing as $\mathcal{J}_{EQ}$. The quantity $\mathcal{J}_{\parallel}^{\mathcal{C}}$ represents the FACs carried on closed field lines, and we similarly define $\mathcal{J}_{\parallel}^{\mathcal{O}}$ to quantify the FACs on open field lines. Defined this way, FACs from the magnetosphere to the ionosphere correspond to $\mathcal{J}_{\parallel}^{\mathcal{C}} > 0$.

Finally, we define

$$\mathcal{J}_{AEJ}(\phi) = \int -J_{H,\phi} \cdot r \sin(\theta) d\theta, \tag{6}$$

where J_H is the height-integrated ionospheric Hall current from the simulation and also at 0.5° spacing. We take this as a proxy for the AEJ and its ground manifestation, albeit an imperfect one as mentioned in the caveats below. Defined this way, westward current, as with the typical dawnside AEJ, corresponds to $\mathcal{J}_{AEJ} > 0$.

The metrics we define above are shown in Figure 9. However, before interpreting these metrics there are several caveats to bear in mind. The plots are defined using MLT, however the MLT in the ionosphere will not precisely correspond to MLT in the magnetosphere as the magnetic field is not axisymmetric. There can be appreciable bending of magnetic field lines between the ionosphere and magnetosphere, particularly those that originate near the terminator. The plots of ionospheric FACs separate based on field topology and integrate over latitude which may have the effect of concealing some structure. Sunward of the terminator, the closed field region carries the entirety of the R2-sense current while the R1-sense current is carried by both open and closed lines (Wing

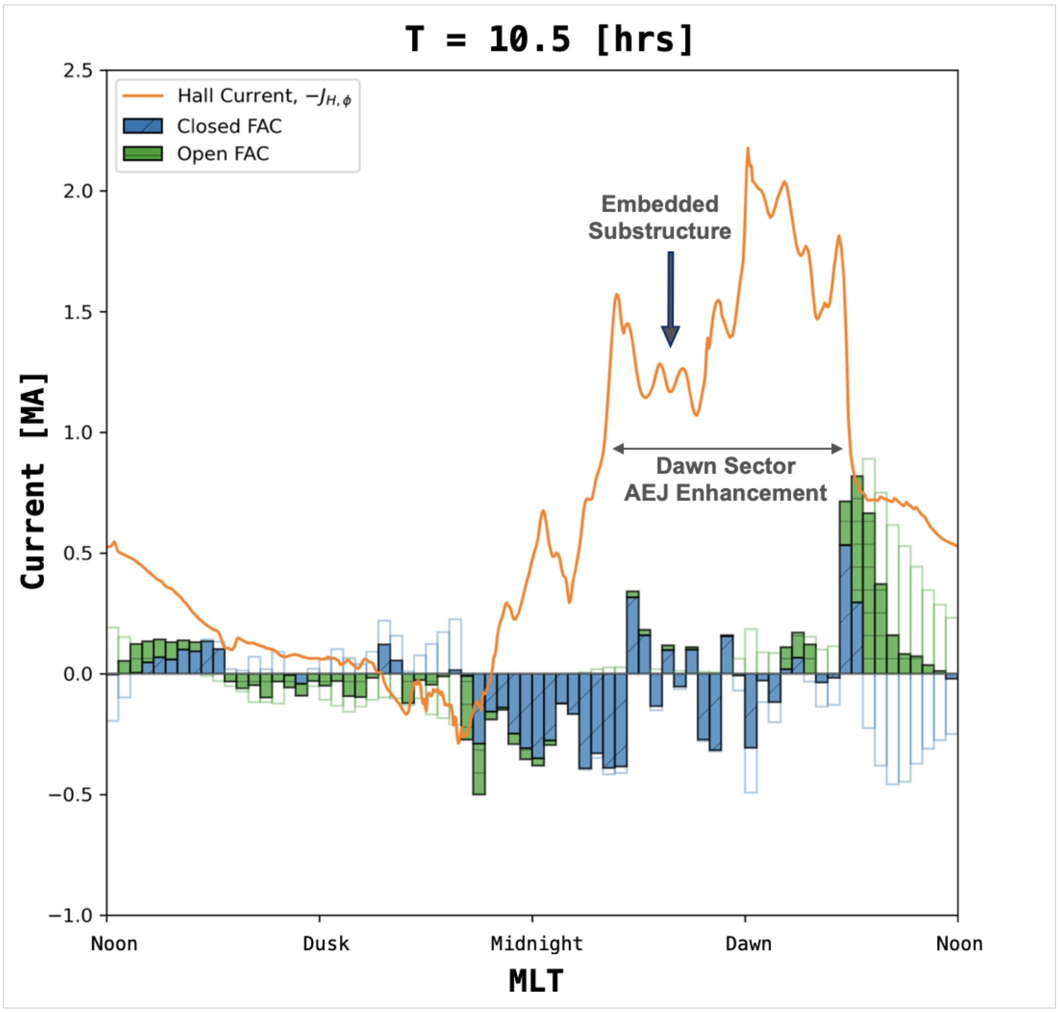

Figure 10. Multiscale enhancement of the dawnside AEJ. Figure depicts similar data as Figure 9 at the marked time (vertical line). Shown are the MLT-profiles of the ionospheric Hall current (line plot, Equation 6) and net FAC, separating open and closed field lines (bar plots, Equation 5) For net FAC, at each MLT if both open and closed contributions are additive, i.e. both upward or downward, the bars are stacked. If the open and closed contributions partially cancel, unshaded bars show the total contribution while the shaded bar shows the net value colored by the dominant contribution.

et al., 2010). By integrating over latitude we see the net polarity of the current: R1-sense on open field lines (Figure 9b), as open lines only carry R1 currents; and R2-sense on closed field lines (Figure 9c), as closed lines carry all the R2-sense currents and a portion of the R1-sense. Finally, we use the ionospheric Hall current as a proxy of the AEJ while a more appropriate choice might be the divergence-free portion of the total, Hall and Pederson, current (eg., Untiedt & Baumjohann, 1993). However, during the period of interest we focus on here, the Pedersen currents are primarily meridional and contribute little to ΔB_N on the ground. We outline these caveats for completeness, but they will not affect our analysis of the geospace currents during the DCW.

Returning now to Figure 9, we consider the evolution of geospace currents and their closure. Recall that the primary DCW we are investigating occurs at 10:30UT, which corresponds to $T = 10.5$ hours in the units shown. Prior to this, we see two important features in the magnetospheric currents (Figure 9). The first is that at $T \lesssim 9.75$ hours there is an intensification of the current centered at midnight. This is followed by an abrupt depletion of the magnetospheric currents predominantly in the post-midnight sector. Considering this in the context of Figure 5, which depicts a very dawn-biased dipolarization, we can interpret this as a substorm-like process which includes a nightside current intensification and subsequent disruption, albeit in this case highly asymmetric. At $T \approx$ 11 hours, there is a weak, MLT-symmetric current which corresponds to the MLT-wide dipolarization we find at $R = 6$ in Figure 6. We will return to the interpretation of the magnetospheric processes in Section 4, but for now merely note that we find the chain of events: intensification of the nightside currents, depletion or disruption of the dawn sector currents, and finally global dipolarization of the inner magnetosphere.

Next we consider the FACs which connect the magnetosphere and ionosphere. Figure 9b depicts a typical R1-sense polarity throughout the interval, with the main feature being the intensification of the dusk and dawn currents in the period following the dropout of the nightside magnetospheric current intensification ($T \approx 9.75$ to $T \approx 10.5$). The intensified R1-sense current can be interpreted as enhanced return flow from the nightside to the dayside reconnection region. Within the closed field domain we find a similar picture to that shown in Figure 6, namely several R1-sense wedgelets on the dawn side which correspond to the dipolarizing bubbles entering the dawnside inner magnetosphere (Figures 5 and 6b). The evolution of these wedgelets match the timing and location of the depleted nightside magnetospheric current (Figure 9a). Figure S7 shows an equatorial snapshot of ΔB_Z and the ionospheric FACs mapped to the equator to demonstrate that these localized flows generate R1-sense wedgelets.

Now moving to the AEJ currents in the ionosphere, we see from Figure 9d that the enhancements of the dawnside AEJ correspond exactly to the nightside depletion of the magnetospheric currents and appearance of R1-sense wedgelets. There is a high degree of asymmetry between the dusk and dawn AEJs, with alternating periods of dawn versus dusk AEJ enhancement. Overall, the dawn AEJ enhancements are appreciably larger in magnitude than those at dusk. We find a strong enhancement of the dawnside AEJ at $T = 10.5$ hours, and further that this enhancement is multiscale. There is an overall enhancement across the dawn quadrant and embedded, localized enhancements colocated with the wedgelets.

To better show the multiscale nature of the AEJ enhancement, Figure 10 depicts what is effectively the information in Figures 9b–d, at $T = 10.5$ hours. From this we can clearly see the main AEJ enhancement extends from midnight to pre-noon and has a feeding current coming from both open and closed field lines and drainage current on closed field lines throughout the pre-dawn sector, with primary drainage current near midnight. Within the overall enhancement there is embedded substructure that correlates with the wedgelets we have identified as coming from BBFs. Figure S11, and its animated counterpart Movie S2, show similar information as Figure 10, but as a $2D$ snapshot in the ionosphere. Finally, of note is the fact that we do not find substantial feeding current coming from the post-noon closed field region, which would be expected if the asymmetric ring current was directly entering and closing through the ionosphere to create the AEJ enhancement.

4 Discussion

4.1 Physical Interpretation

With our main analysis complete, we now seek to interpret the geospace processes at play during the DCW. To better guide the eye we show in Figure 11 a more visual representation of the information in Figure 9 at two snapshots in time, before and dur-

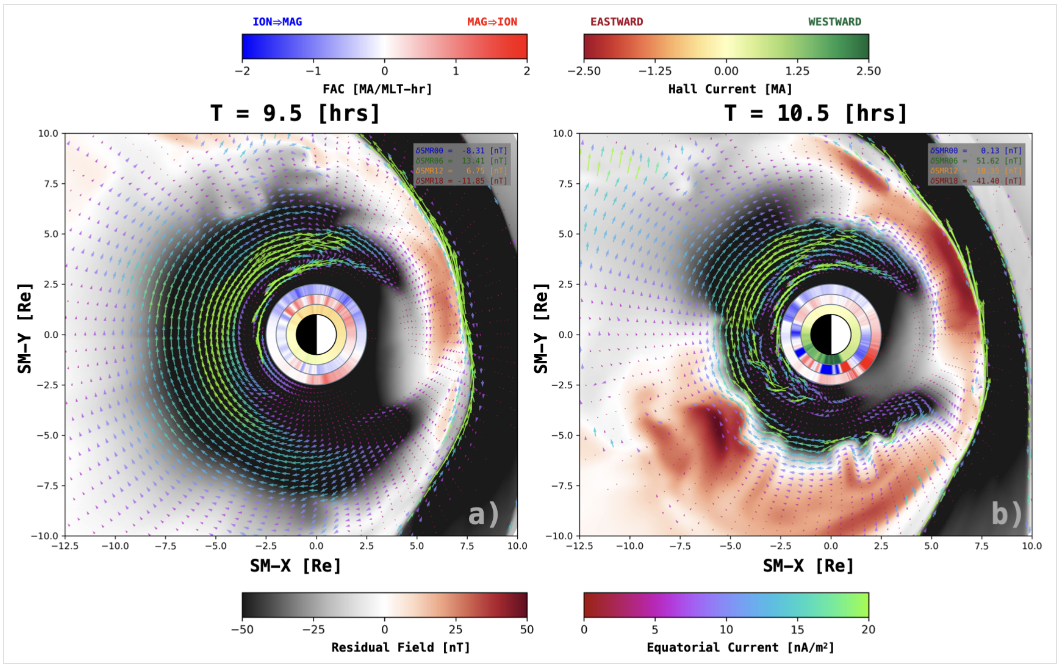

Figure 11. Visualization of geospace currents before (a) and during (b) the DCW. Shown are the residual magnetic field in the magnetospheric equator with arrows used to depict the equatorial currents. Inset rings around Earth show, from outwards to in: FACs on open field lines, FACs on closed field lines, and the ionospheric Hall current. An animated version of this Figure is available in Movie S3.

ing the DCW. In Figure 11 we depict the magnetospheric currents in the equator and in the 3 dial plots around Earth, moving from outwards to inwards, we show the FACs on open and closed lines and in the innermost ring the ionospheric Hall current. In other words, the three dial plots show the data in Figures 9b-d. An animated version of the visualization in Figure 11 is presented in Movie S3, and Movie S2 shows the latitudinal structure of the AEJ and FACs.

Starting in the magnetotail, we see a clear difference in the cross-tail current between Figures 11a and b. Specifically, we find the disappearance of the cross-tail current in the post-midnight tail and inward-propagating dipolarizing flows (see also Movie S3). Figure 11b highlights the connection between the magnetospheric bubbles and the MI coupling: the feeding current coming from both open and closed field lines pre-noon; the primary drainage current near midnight, coinciding with the duskside cross-tail current that is still present; and the wedgelet currents associated with individual flow structures. From Figure 11b we can also see a largely dipolarized inner magnetosphere near noon, equivalent to there being negligible equatorial current in that location, and that the westward edge of the duskside ring current is not associated with any strong FACs in the closed field region. This shows that the ring current does not flow from dusk past noon into the dawn sector, nor is it providing a substantial feeding current to the dawnside AEJ by closing through the ionosphere. This suggests that the primary closure of the asymmetric ring current is through the eastward banana current (Liemohn et al., 2013) and/or the magnetopause. Unlike in the PRC model of Fukushima and Kamide (1973) we find that the asymmetric ring current is not *directly* responsible for the dawnside AEJ enhancement. However, we will argue that the asymmetric ring current plays an important indirect, and ultimately causal role in the dawnside AEJ enhancement.

The asymmetric disruption of the cross-tail current suggests a substorm-like process, but biased to the dawnside. Evidence for this can be seen in Figure 12, which shows the cross-tail current J_Y in the $X = -10\ R_E$ plane before, during, and after the DCW. Prior to the DCW (Figure 12a), there is an intense cross-tail current with half-thickness $\approx 0.5\ R_E$. During the DCW (Figure 12b), where the $SML06$ is near its local minimum (Figure 4) there are signatures of a substorm but confined the dawnside. We note the abrupt disappearance of the dawnside cross-tail current and the expansion of the dawnside magnetotail. The duskside magnetotail paints quite a different picture, with the cross-tail current largely similar to the pre-DCW configuration. This is consistent with our identification of the draining current of the DCW occuring at midnight (Figure 10) and the persistence of the duskside cross-tail current we find in Figure 9a and Figure 11b. This asymmetry soon disappears, as we find 30 minutes later a symmetric, more inflated magnetotail (Figure 12c). This post-onset configuration is coincident with the local minima of dawn-dusk SMR asymmetry, i.e. $\Delta_{18}^{06} SMR$.

The unusual magnetotail configuration depicted in Figure 12 invites the question as to why such an asymmetric substorm-like process might arise in the first place. Here we find that the preceding asymmetric ring current configuration suggests an answer. Previous work has suggested that the magnetic perturbation produced by the ring current may inhibit reconnection in the magnetotail (Nakai & Kamide, 2003; Milan et al., 2009, 2021). Intuitively, we would expect a westward current segment in the equator to lead to a $\Delta B_Z > 0$ tailwards of the segment. In other words, the westward ring current inflates the magnetotail which inhibits reconnection. The asymmetric spatial distribution of the ring current during the main phase, biased towards dusk, leads to an asymmetric inflation of the tail and, potentially, asymmetric reconnection when it does occur. For reconnection happening far tailward of the ring current this asymmetry may have minimal impact. However, as the reconnection location moves earthward the impact of the asymmetric tailward inflation due to the ring current would be magnified due to the increased proximity.

Recent observational work has identified near-Earth ($\lesssim 10R_E$) reconnection during intense storms (Angelopoulos et al., 2020; Runov et al., 2022). In the context of our simulation, we find that reconnection begins at $X \approx -15R_E$ (Movie S1, 10:10UT) which is Earthward of typical non-stormtime values, for which $X \approx -25R_E$ is more representative (e.g., Nagai et al., 1998). Prior modeling work has shown that near-Earth reconnection produces more depleted bubbles, capable of deeper penetration into the inner magnetosphere (Lopez et al., 2009). In other words, if near-Earth reconnection were to occur in the presence of a dusk-biased ring current that would lead to particularly entropy-depleted, and therefore buoyant, dawnside bubbles. This suggests the sequence: dusk-biased RC leading to a dawn-biased substorm-like process, which leads to dawnside ion transport that reestablishes dawn-dusk symmetry in the RC. In this way, strong dawn-dusk asymmetry in the ring current may be, at least partially, self-regulating.

Our interpretation should not be taken to suggest that any stormtime reconnection would be dawnward-biased, as the ring current is not always asymmetric during the main phase and reconnection occurring far tailward of the ring current would be less affected by asymmetric inflation. Yet this interpretation does explain why dawnside bias would occur sporadically during the main phase of geomagnetic storms. Recent work has increasingly highlighted the role of the dawnside near-Earth plasma sheet magnetosphere during active periods. Adewuyi et al. (2021) used ground measurements in tandem with ENA and auroral imaging to study plasma sheet flows during a geomagnetic storm. During the storm main phase, they identified numerous mesoscale flow channels that exhibited a post-midnight bias. The importance of ion access to the dawnside inner magnetosphere during geomagnetically active times was also highlighted by (Lin et al., 2022) in their recent work explaining ”dawnside SAPS”.

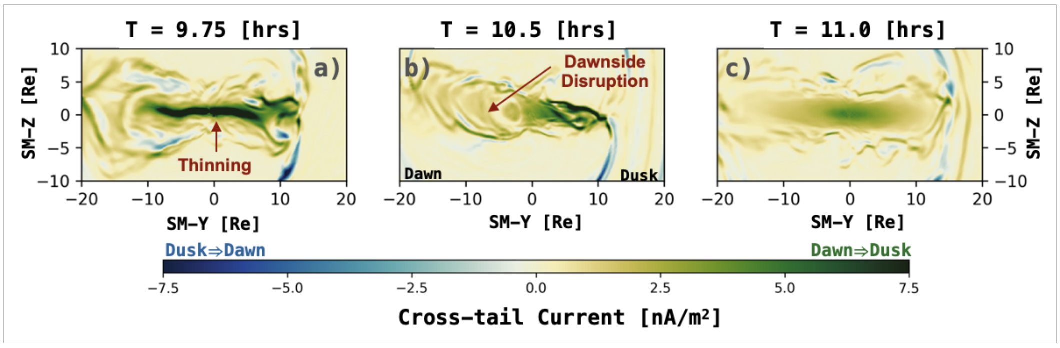

Figure 12. Evolution of the cross-tail current. Shown is the dawn-dusk oriented magnetospheric current, J_Y, in the SM-YZ plane taken at $X = -10\ R_E$at times taken before (a), during (b), and after (c) the DCW.

Before moving on, we summarize our interpretation here. The precursor to the DCW is the development of a strongly dusk-biased ring current, a typical occurrence during storm main phase. This leads to asymmetric inflation of the magnetotail and the preference for dawnside reconnection. When reconnection onset occurs, it is highly dawn-biased and results in strong flows on the dawnside, which transport magnetic flux and energetic particles. That transport occurs primarily in the form of mesoscale, dipolarizing bubbles. The enhanced sunward flow from the dawnside magnetotail extends from the plasma sheet flanks, which generates an eastward-propagating enhanced R1-sense current, to the near-midnight flow that is diverted eastward around the inner magnetosphere, which generates enhanced R2-sense current near midnight. These are the feeding and drainage currents, with their ionospheric closure through the AEJ mediated by the R1-sense wedgelets of the bubbles. The analysis we have conducted in this case study of the DCW has centered on a unique kind of substorm-like process which would be expected to occur primarily during the main phase of geomagnetic storms.

Ohtani et al. (2022) suggest four, non-exclusive scenarios for the DCW: dayside compression, enhanced convection, substorm onset, and electron injections. Within the picture we find here, each of these processes can play a role as either causal, preceding, or secondary. As we describe above, our simulation suggests the onset of the dawnside-biased substorm -like process to be causal. Bubbles carrying energetic electrons into the inner magnetosphere, while not the originating effect, create an eastward-propagating conductance enhancement through their precipitation. This effect can reinforce and augment the dawnward bias of the initial reconnection and trajectory of subsequent bubbles. In this way, if the substorm-like process is causal then electron injections are a secondary contributing factor. Both compression and enhanced convection can be interpreted as preceding, in that both can lead to a highly dusk-biased ring current. Dayside compression causes the magnetopause to intersect ion drift orbits and results in magnetopause shadowing, the pre-noon absence of westward-drifting ions which escape the magnetosphere through the magnetopause in the post-noon sector (Sibeck et al., 1987; Ohtani et al., 2007). Enhanced convection transports ions into the near-Earth plasma sheet where their tendency to drift westward also leads to duskward-bias.

4.2 Space Weather Implications

Turning away from the physical interpretation, we now consider the space weather implications of our results. Using a GIC measurement system deployed at high geomagnetic latitude, Apatenkov et al. (2020) found that the strongest GIC event over the 8 year

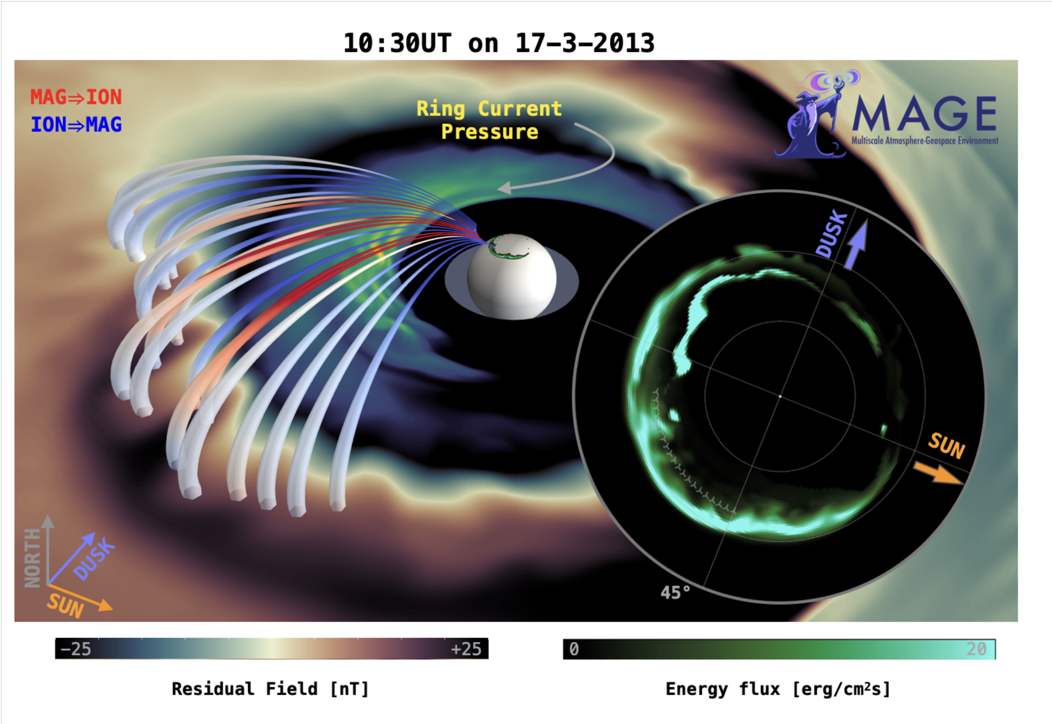

Figure 13. Dawnside BBFs and auroral Omega band during the DCW. Shown is a $3D$ snapshot of the simulation at 10:30 depicting equatorial residual field and the precipitating electron energy flux into the ionosphere (inset). Field lines are traced from the ionosphere to the magnetosphere at an arc of constant latitude, with their seed points marked in the ionospheric inset. The traced field lines are colored by FAC, with red and blue denoting downward and upward currents, respectively.

monitoring period (2011-2019) occurred in the dawn sector during a geomagnetic storm. Large-amplitude dB/dt values are connected to space weather induced GIC hazards (Pulkkinen et al., 2017) and dB/dt itself has been proposed as a metric for an emergency alert framework (Kataoka & Ngwira, 2016). Statistical studies of dB/dt spikes in ground magnetometer data have shown local time hotspots in the dawn sector (Schillings et al., 2022; Milan et al., 2023). In addition to temporal variability, spatial variability has also been a subject of operational interest as hazardous GEFs can be highly localized (Pulkkinen, 2015; Ngwira et al., 2015; Engebretson, Steinmetz, et al., 2019). An operational study by EPRI (EPRI, 2020) confirmed that localized enhancements, defined as several hundred km, should be considered in GIC hazard assessments in the auroral zone. Further, they found that localized GEF enhancements primarily occur in the pre-dawn sector, 3-6 MLT. Numerous studies have connected hazardous dawnside conditions to auroral activity, specifically dawnside Omega bands (Apatenkov et al., 2020; Schillings et al., 2022; Milan et al., 2023; Zou et al., 2022). Omega bands are an auroral form exhibiting mesoscale undulations on the poleward edge of the auroral oval (see Forsyth et al., 2020, and references therein), and have been interpreted as the auroral manifestation of BBFs (Henderson et al., 2002; Andreeva et al., 2021).

The DCW mediated by BBFs/bubbles would explain the dawnside hotspot of large-amplitude dB/dt and the pre-dawn preference of localized GEF enhancements. The connection between dawnside dB/dt and Omega bands would also be explained by the DCW with a mesoscale makeup. Figure 13 shows a $3D$ snapshot of the simulation during the

DCW and the precipitating electron energy flux, used in the calculation of the ionospheric conductance, as a simple auroral proxy. We find that the DCW in our model produces an ionospheric signature consistent with Omega bands and show with field line tracing the connection between the Omega band auroral form and the dawnside bubbles.

Lastly, we remark that in our interpretation (Section 4.1) we find that dawn-dusk ring current asymmetry is the causal factor of the DCW. This suggests that large values of $\Delta_{18}^{06}SMR$, the dawn-dusk SMR asymmetry, during geomagnetically disturbed periods could be a leading indicator of potentially hazardous dB/dt in the dawn quadrant auroral zone within the next hour. A detailed study of the connection between $\Delta_{18}^{06}SMR$ and dB/dt is beyond the scope of this paper. However, we show here a very simple example of how these may be connected. To this end we construct a dB/dt index analogous to *SML*-LT. Specifically, we define

$$\dot{B}(UT, MLT) = \max_{s \in \mathcal{S}} \| \frac{\partial \vec{B}^s}{\partial t} \|, \tag{7}$$

where $\vec{B}^s$ is the magnetic field measurement at a given station and at each MLT bin $\mathcal{S}$ are the stations used to calculate the *SML*-LT at that MLT. In other words, we are using sliding MLT windows over auroral magnetometer stations and calculating the largest measured magnetic field variation.

We show in Figure 14a and Figure 14b an example of this dB/dt index compared with *SMR*06 and *SMR*18 for the event that we have chosen for our case study. We note that this is using the SuperMAG data, and not the synthetic measurements from the model. For this event the largest and most persistent ground variability occurs in the dawn sector and that there does appear to be a correlation between dawn-dusk *SMR* asymmetry, $\Delta_{18}^{06}SMR$ and dawnside ground variability, $\dot{B}$-06. To better highlight this relationship, Figure 14c depicts the two time series: $\Delta_{18}^{06}SMR$ and $\dot{B}$-06, the latter of which is plotted with both the direct calculation and with a 15 minute temporal smoothing window. We calculate the two time series to have a correlation coefficient, *c.c.* $= +0.69$. We stress, however, that this is just a simple estimate taken from one event. Larger studies utilizing more sophisticated correlation analysis would be necessary to demonstrate a robust correlative, and/or causal, relationship between these geomagnetic indices.

5 Conclusions

We have presented here a case study of the dawnside current wedge (DCW). Ohtani (2021), using SuperMAG statistics from hundreds of geomagnetic storms, identified a robust correlation between low- and mid-latitude asymmetry in the ground magnetic depression and the enhancement of the dawnside AEJ. They interpreted this as a wedge current system centered at dawn, the DCW. The ubiquity of the DCW during stormtime and connection to a persistent stormtime characteristic, namely the dawn-dusk ring current asymmetry, suggests the DCW is an important aspect of stormtime MI coupling. As such, we wish to verify that our global geospace model is able to reproduce this persistent, recurrent aspect of stormtime geospace. To this end, we have used the well-studied March 2013 "St. Patrick's Day" geomagnetic storm as a case study to investigate the DCW using the MAGE model. Using synthetic SuperMAG indices calculated from the model, we have showed that the model is able to reproduce:

- Equatorial and auroral geomagnetic indices, with MLT granularity (Figures 1 and 2)
- The dawn-dusk asymmetry in SMR, specifically: onset times, interval durations, and approximate magnitudes (Figure 3)
- The core phenomenology of the DCW, namely the correlation between dawn-dusk *SMR* asymmetry and enhancement of the dawnside AEJ, proxied by *SML*06 (Figure 4).

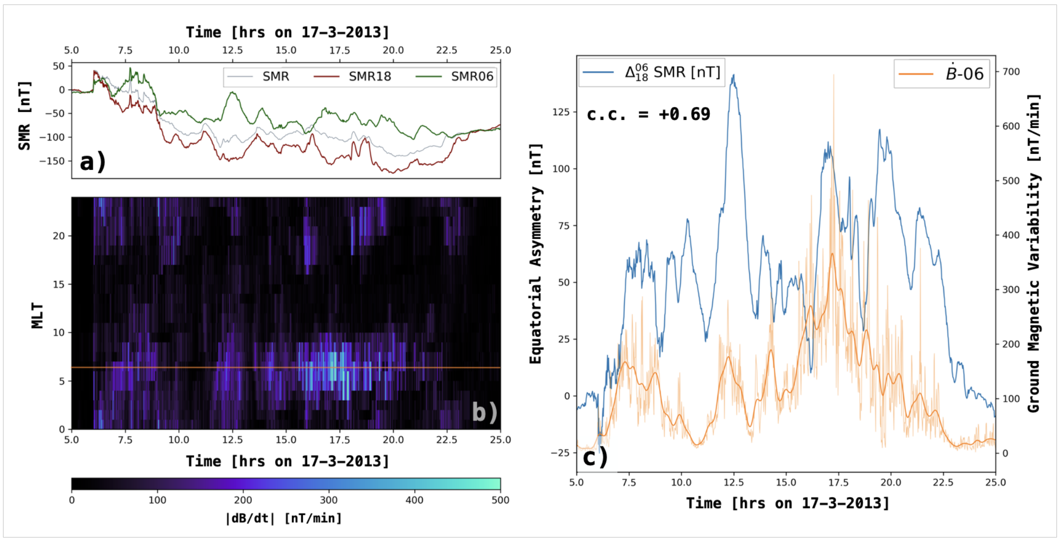

Figure 14. Connection between dawn-dusk ring current asymmetry and ground magnetic variability. Shown on the left are the time evolution of $SMR06$ and $SMR18$ (panel a) and the ground magnetic variability index described by Equation 7 (panel b). On the right (panel c), we show the ground magnetic variability at dawn (as marked in panel b, orange line) with and without a 15 minute temporal smoothing window as well as the dawn-dusk ring current asymmetry, $\Delta^{06}_{18}SMR$ (Equation 2). The correlation coefficient between the two time series is +0.69. Note, all the data shown in this plot are derived from SuperMAG measurements, not synthetic quantities from the model.

To investigate the underlying processes at play during the DCW, we chose a fiducial DCW at 10:30UT, the period of peak dawn-dusk asymmetry and minimum SML (Figure 4). In the model, this period was characterized by:

- Dawnside disruption of the cross-tail current in the magnetosphere preceded by a period of symmetric thinning of the magnetotail (Figures 9a, and 12b)
- Dipolarizing, entropy-depleted BBFs/bubbles penetrating the dawnside inner magnetosphere preceding an MLT-wide dipolarization (Figures 6b, and S4)
- R1-sense wedgelets spanning the dawnside inner magnetosphere and disrupting the dawnside R2 current system (Figure 6c)
- Global enhancement and eastward expansion of the dawnside AEJ (Figure 2d) with embedded substructure corresponding to the R1-sense wedgelets of dawnside BBFs/bubbles (Figure 10).

Based on our analysis, we then provided an interpretation of the DCW that connects stormtime dawn-dusk asymmetry of the ring current to dawnside AEJ enhancements (Section 4.1). We suggest that the development of a dusk-biased ring current asymmetrically inflates the magnetotail. This dusk-biased inflation inhibits duskside reconnection, which results in a dawn-biased substorm-like process (Figure 12b). The dawnside reconnection launches mesoscale bubbles across the dawnside plasma sheet and into the inner magnetosphere, which creates a multiscale enhancement of the AEJ (Figure 10). An important caveat here is that this interpretation is based on our case study. For the DCW, this is the first modeling investigation of any kind. Wider studies of stormtime MI-coupling are necessary to confirm our interpretation and to better quantify the relative role of different contributing factors.

Finally, while our primary focus here has been on the physical understanding of stormtime MI coupling, we have also discussed potential space weather implications of the DCW (Section 4.2). Using an auroral proxy from the model, we find that the DCW creates signatures consistent with dawnside Omega bands (Figure 13). This suggests that the DCW can explain prior statistical work which found that there was a statistical hotspot of large ground dB/dt in the morning sector associated with dawnside Omega bands (Schillings et al., 2022). Further, the embedded substructure that we find in the dawnside AEJ enhancement may explain why localized GEFs primarily occur in the pre-dawn sector (EPRI, 2020). To support this, we calculate a simple dB/dt index analogous to *SML*-LT (Figure 14) and show that there is a correlation between dawn-dusk asymmetry in *SMR* and large dB/dt on the ground at dawn.

6 Open Research

Full simulation output during the period of our primary analysis, 10:00-11:00 UT, stored at reduced cadence is included in Dataset S1 (K. Sorathia, 2023) and is available online at Zenodo (via https://doi.org/10.5281/zenodo.8178574). This includes output from the magnetospheric, ionospheric, and inner magnetosphere models. The MAGE output data can be analyzed using a publicly available Python module (CGS, 2023), available at `https://pypi.org/project/kaipy/`, or interactively visualized using open source scientific data visualization tools like ParaView (kitware, 2023) or VisIt (Childs et al., 2023). The format of the files and their contents are described in the Supplementary Information, which also includes an example Python script.

Acknowledgments

This work is supported by the NASA DRIVE Science Center for Geospace Storms (CGS) under award 80NSSC22M0163, and NASA grants 80NSSC19K0241, 80NSSC20K1833, and 80NSSC17K0679. V.G.M. acknowledges support from NASA grants 80NSSC19K0071 and 80NSSC19K0080. S.O. acknowledges support from NASA grant 80NSSC21K0036. A.M. was supported by the NASA Early Career Investigator Program, grant 80NSSC21K0464. A.K. acknowledges support from NASA grants 80NSSC19K0755, 80NSSC20K0701, and 80NSSC22K0802 as well as NSF award AGS-2109543. C.R. was supported by the BMBWF grant "Digitale und soziale Transformation in der Hochschule" - "Austrian DataLAB and Services"

We gratefully acknowledge use of NASA/GSFC's Space Physics Data Facility's OMNIWeb service, and OMNI data as well as SuperMAG and its collaborators (`https://supermag.jhuapl.edu/info/?page=acknowledgement`). Computational resources were provided by NCAR's Computational and Information Systems Laboratory, sponsored by the National Science Foundation and performed on the Cheynne supercomputer (doi:10.5065/D6RX99HX).

References

Adewuyi, M., Keesee, A. M., Nishimura, Y., Gabrielse, C., & Katus, R. M. (2021). Mesoscale Features in the Global Geospace Response to the March 12, 2012 Storm. *Frontiers in Astronomy and Space Sciences*, *8*. Retrieved 2023-02-22, from `https://www.frontiersin.org/articles/10.3389/fspas.2021.746459`

Anderson, B. J., Korth, H., Waters, C. L., Green, D. L., Merkin, V. G., Barnes, R. J., & Dyrud, L. P. (2014, May). Development of large-scale Birkeland currents determined from the Active Magnetosphere and Planetary Electrodynamics Response Experiment: DEVELOPMENT OF BIRKELAND CURRENTS. *Geophysical Research Letters*, *41*(9), 3017–3025. Retrieved 2023-03-16, from `http://doi.wiley.com/10.1002/2014GL059941` doi:

10.1002/2014GL059941

Andreeva, V. A., Apatenkov, S. V., Gordeev, E. I., Partamies, N., & Kauristie, K. (2021, June). Omega Band Magnetospheric Source Location: A Statistical Model-Based Study. *Journal of Geophysical Research: Space Physics*, *126*(6). Retrieved 2023-03-01, from https://onlinelibrary.wiley.com/doi/10.1029/2020JA028997 doi: 10.1029/2020JA028997

Angelopoulos, V., Artemyev, A., Phan, T. D., & Miyashita, Y. (2020, January). Near-Earth magnetotail reconnection powers space storms. *Nature Physics*, *99*, 1 – 5. Retrieved from https://www.nature.com/articles/s41567-019-0749-4 doi: 10.1038/s41567-019-0749-4

Angelopoulos, V., Baumjohann, W., Kennel, C. F., Coroniti, F. V., Kivelson, M. G., Pellat, R., ... Paschmann, G. (1992, April). Bursty bulk flows in the inner central plasma sheet. *Journal of Geophysical Research*, *97*(A4), 4027 – 4039. Retrieved from http://onlinelibrary.wiley.com/doi/10.1029/91JA02701/full doi: 10.1029/91ja02701

Apatenkov, S. V., Pilipenko, V. A., Gordeev, E. I., Viljanen, A., Juusola, L., Belakhovsky, V. B., ... Selivanov, V. N. (2020). Auroral Omega Bands are a Significant Cause of Large Geomagnetically Induced Currents. *Geophysical Research Letters*, *47*(6), e2019GL086677. Retrieved 2023-07-13, from https://onlinelibrary.wiley.com/doi/abs/10.1029/2019GL086677 (_eprint: https://onlinelibrary.wiley.com/doi/pdf/10.1029/2019GL086677) doi: 10.1029/2019GL086677

Baumjohann, W., Paschmann, G., & Lühr, H. (1990). Characteristics of high-speed ion flows in the plasma sheet. *Journal of Geophysical Research: Space Physics (1978–2012)*, *95*(A4), 3801–3809. doi: 10.1029/ja095ia04p03801

Borovsky, J. E., Thomsen, M. F., & Elphic, R. C. (1998, August). The driving of the plasma sheet by the solar wind. *Journal of Geophysical Research*, *103*(A), 17617 – 17640. doi: 10.1029/97ja02986

CGS. (2023). *Kaipy [software].* Retrieved from https://pypi.org/project/kaipy/

Childs, H., Brugger, E., Whitlock, B., Meredith, J., Ahern, S., Pugmire, D., ... Navrátil, P. (2023). *Visit [software].* Retrieved from https://wci.llnl.gov/simulation/computer-codes/visit/

Chu, X., McPherron, R. L., Hsu, T.-S., Angelopoulos, V., Pu, Z., Yao, Z., ... Connors, M. (2015, January). Magnetic mapping effects of substorm currents leading to auroral poleward expansion and equatorward retreat: Mapping effect causing auroral expansion. *Journal of Geophysical Research: Space Physics*, *120*(1), 253–265. Retrieved 2023-03-16, from http://doi.wiley.com/10.1002/2014JA020596 doi: 10.1002/2014JA020596

Dessler, A. J., & Parker, E. N. (1959). Hydromagnetic theory of geomagnetic storms. *Journal of Geophysical Research*, *64*(12), 2239–2252. doi: 10.1029/jz064i012p02239

Ebihara, Y., Ejiri, M., Nilsson, H., Sandahl, I., Milillo, A., Grande, M., ... Roeder, J. L. (2002, October). Statistical distribution of the storm-time proton ring current: POLAR measurements: STORM-TIME PROTON RING CURRENT. *Geophysical Research Letters*, *29*(20), 30–1–30–4. Retrieved 2023-03-14, from http://doi.wiley.com/10.1029/2002GL015430 doi: 10.1029/2002GL015430

Engebretson, M. J., Pilipenko, V. A., Ahmed, L. Y., Posch, J. L., Steinmetz, E. S., Moldwin, M. B., ... Vorobev, A. V. (2019, September). Nighttime Magnetic Perturbation Events Observed in Arctic Canada: 1. Survey and Statistical Analysis. *Journal of Geophysical Research: Space Physics*, *124*(9), 7442–7458. Retrieved 2023-03-14, from https://onlinelibrary.wiley.com/doi/10.1029/2019JA026794 doi: 10.1029/2019JA026794

Engebretson, M. J., Steinmetz, E. S., Posch, J. L., Pilipenko, V. A., Moldwin, M. B., Connors, M. G., … Kistler, L. M. (2019, September). Nighttime Magnetic Perturbation Events Observed in Arctic Canada: 2. Multiple-Instrument Observations. *Journal of Geophysical Research: Space Physics*, *124*(9), 7459–7476. Retrieved 2023-03-14, from https://onlinelibrary.wiley.com/doi/10.1029/2019JA026797 doi: 10.1029/2019JA026797

EPRI. (2020). *Furthering the Understanding of the Characteristics and Scales of Geoelectric Field Enhancements* (Tech. Rep. No. 3002017900). Palo Alto, CA: Author.

Fejer, J. A. (1961, October). The effects of energetic trapped particles on magnetospheric motions and ionospheric currents. *Canadian Journal of Physics*, *39*(10), 1409–1417. Retrieved 2023-02-27, from https://cdnsciencepub.com/doi/10.1139/p61-168 (Publisher: NRC Research Press) doi: 10.1139/p61-168

Forsyth, C., Sergeev, V. A., Henderson, M. G., Nishimura, Y., & Gallardo-Lacourt, B. (2020, April). Physical Processes of Meso-Scale, Dynamic Auroral Forms. *Space Science Reviews*, *216*(4), 46. Retrieved 2022-07-14, from https://doi.org/10.1007/s11214-020-00665-y doi: 10.1007/s11214-020-00665-y

Fukushima, N., & Kamide, Y. (1973). Partial ring current models for worldwide geomagnetic disturbances. *Reviews of Geophysics*, *11*(4), 795–853. Retrieved 2023-02-13, from https://onlinelibrary.wiley.com/doi/abs/10.1029/RG011i004p00795 (_eprint: https://onlinelibrary.wiley.com/doi/pdf/10.1029/RG011i004p00795) doi: 10.1029/RG011i004p00795

Gallagher, D. L., Craven, P. D., & Comfort, R. H. (2000, August). Global core plasma model. *Journal of Geophysical Research*, *105*(A8), 18819 – 18833. Retrieved from https://agupubs.onlinelibrary.wiley.com/doi/abs/10.1029/1999JA000241 doi: 10.1029/1999ja000241

Gjerloev, J. W. (2012). The SuperMAG data processing technique. *Journal of Geophysical Research: Space Physics*, *117*(A9). Retrieved 2022-08-30, from https://onlinelibrary.wiley.com/doi/abs/10.1029/2012JA017683 (_eprint: https://onlinelibrary.wiley.com/doi/pdf/10.1029/2012JA017683) doi: 10.1029/2012JA017683

Henderson, M. G., Kepko, L., Spence, H. E., Connors, M., Sigwarth, J. B., Frank, L. A., … Yumoto, K. (2002, January). *The Evolution of North-South Aligned Auroral Forms into Auroral Torch Structures : The Generation of Omega Bands and Ps6 Pulsations via Flow Bursts.* (Tech. Rep. No. LA-UR-02-3972). Los Alamos National Lab. (LANL), Los Alamos, NM (United States). Retrieved 2023-03-01, from https://www.osti.gov/biblio/976215

Iijima, T., & Potemra, T. A. (1976). The amplitude distribution of field-aligned currents at northern high latitudes observed by Triad. *Journal of Geophysical Research (1896-1977)*, *81*(13), 2165–2174. Retrieved 2023-02-28, from https://onlinelibrary.wiley.com/doi/abs/10.1029/JA081i013p02165 (_eprint: https://onlinelibrary.wiley.com/doi/pdf/10.1029/JA081i013p02165) doi: 10.1029/JA081i013p02165

Ilie, R., Skoug, R. M., Funsten, H. O., Liemohn, M. W., Bailey, J. J., & Gruntman, M. (2013, July). The impact of geocoronal density on ring current development. *Journal of Atmospheric and Solar-Terrestrial Physics*, *99*, 92–103. Retrieved 2023-01-04, from https://www.sciencedirect.com/science/article/pii/S1364682612000946 doi: 10.1016/j.jastp.2012.03.010

Kaeppler, S. R., Hampton, D. L., Nicolls, M. J., Strømme, A., Solomon, S. C., Hecht, J. H., & Conde, M. G. (2015). An investigation comparing ground-based techniques that quantify auroral electron flux and conductance. *Journal of Geophysical Research: Space Physics*, *120*(10), 9038–9056. doi: 10.1002/2015ja021396

Kataoka, R., & Ngwira, C. (2016, August). Extreme geomagnetically induced currents. *Progress in Earth and Planetary Science*, *3*(1), A09226 – 7. Retrieved from https://progearthplanetsci.springeropen.com/articles/10.1186/s40645-016-0101-x doi: 10.1186/s40645-016-0101-x

Keesee, A. M., Buzulukova, N., Mouikis, C., & Scime, E. E. (2021). Mesoscale Structures in Earth's Magnetotail Observed Using Energetic Neutral Atom Imaging. *Geophysical Research Letters*, *48*(3), e2020GL091467. Retrieved 2022-06-15, from https://onlinelibrary.wiley.com/doi/abs/10.1029/2020GL091467 (_eprint: https://onlinelibrary.wiley.com/doi/pdf/10.1029/2020GL091467) doi: 10.1029/2020GL091467

Keesee, A. M., Chen, M. W., Scime, E. E., & Lui, A. T. Y. (2014, October). Regions of ion energization observed during the Galaxy-15 substorm with TWINS: TWINS Galaxy-15. *Journal of Geophysical Research: Space Physics*, *119*(10), 8274–8287. Retrieved 2023-02-28, from http://doi.wiley.com/10.1002/2014JA020466 doi: 10.1002/2014JA020466

Kepko, L., McPherron, R. L., Amm, O., Apatenkov, S., Baumjohann, W., Birn, J., ... Sergeev, V. (2015). Substorm Current Wedge Revisited. *Space Science Reviews*, *190*(1-4), 1–46. doi: 10.1007/s11214-014-0124-9

kitware. (2023). *Paraview [software]*. Retrieved from https://www.paraview.org/

Korth, A., Friedel, R. H. W., Mouikis, C. G., Fennell, J. F., Wygant, J. R., & Korth, H. (2000). Comprehensive particle and field observations of magnetic storms at different local times from the CRRES spacecraft. *Journal of Geophysical Research: Space Physics*, *105*(A8), 18729–18740. Retrieved 2023-02-10, from https://onlinelibrary.wiley.com/doi/abs/10.1029/1999JA000430 (_eprint: https://onlinelibrary.wiley.com/doi/pdf/10.1029/1999JA000430) doi: 10.1029/1999JA000430

Liemohn, M. W. (2003, June). Yet another caveat to using the Dessler-Parker-Sckopke relation. *Journal of Geophysical Research*, *108*(A6), 641. Retrieved from https://agupubs.onlinelibrary.wiley.com/doi/epdf/10.1029/2003JA009839 doi: 10.1029/2003ja009839

Liemohn, M. W., Ganushkina, N. Y., Katus, R. M., De Zeeuw, D. L., & Welling, D. T. (2013). The magnetospheric banana current. *Journal of Geophysical Research: Space Physics*, *118*(3), 1009–1021. Retrieved 2023-02-10, from https://onlinelibrary.wiley.com/doi/abs/10.1002/jgra.50153 (_eprint: https://onlinelibrary.wiley.com/doi/pdf/10.1002/jgra.50153) doi: 10.1002/jgra.50153

Lin, D., Sorathia, K., Wang, W., Merkin, V., Bao, S., Pham, K., ... Anderson, B. (2021). The Role of Diffuse Electron Precipitation in the Formation of Subauroral Polarization Streams. *Journal of Geophysical Research: Space Physics*, *126*(12), e2021JA029792. Retrieved 2022-07-22, from https://onlinelibrary.wiley.com/doi/abs/10.1029/2021JA029792 (_eprint: https://onlinelibrary.wiley.com/doi/pdf/10.1029/2021JA029792) doi: 10.1029/2021JA029792

Lin, D., Wang, W., Merkin, V. G., Huang, C., Oppenheim, M., Sorathia, K., ... Garretson, J. (2022). Origin of Dawnside Subauroral Polarization Streams During Major Geomagnetic Storms. *AGU Advances*, *3*(4), e2022AV000708. Retrieved 2022-11-07, from https://onlinelibrary.wiley.com/doi/abs/10.1029/2022AV000708 (_eprint: https://onlinelibrary.wiley.com/doi/pdf/10.1029/2022AV000708) doi: 10.1029/2022AV000708

Lindsay, B. G., & Stebbings, R. F. (2005, December). Charge transfer cross sections for energetic neutral atom data analysis. *Journal of Geophysical Research: Space Physics*, *110*(A), A12213. doi: 10.1029/2005ja011298

Liu, J., Angelopoulos, V., Runov, A., & Zhou, X. (2013). On the current sheets surrounding dipolarizing flux bundles in the magnetotail: The case for wedgelets.

Journal of Geophysical Research: Space Physics, *118*(5), 2000–2020. doi: 10.1002/jgra.50092

Lopez, R. E., Lyon, J. G., Mitchell, E., Bruntz, R., Merkin, V. G., Brogl, S., . . . Wiltberger, M. (2009). Why doesn't the ring current injection rate saturate? *Journal of Geophysical Research: Space Physics (1978–2012)*, *114*(A2), n/a–n/a. doi: 10.1029/2008ja013141

Lyon, J. G., Fedder, J. A., & Mobarry, C. M. (2004, October). The Lyon–Fedder–Mobarry (LFM) global MHD magnetospheric simulation code. *Journal of Atmospheric and Solar-Terrestrial Physics*, *66*(15-16), 1333 – 1350. doi: 10.1016/j.jastp.2004.03.020

McComas, D. J., Allegrini, F., Baldonado, J., Blake, B., Brandt, P. C., Burch, J., . . . Zoennchen, J. (2009, February). The Two Wide-angle Imaging Neutral-atom Spectrometers (TWINS) NASA Mission-of-Opportunity. *Space Science Reviews*, *142*(1-4), 157–231. Retrieved 2023-02-28, from http://link.springer.com/10.1007/s11214-008-9467-4 doi: 10.1007/s11214-008-9467-4

Merkin, V. G., & Lyon, J. G. (2010). Effects of the low-latitude ionospheric boundary condition on the global magnetosphere. *Journal of Geophysical Research: Space Physics*, *115*(A10). Retrieved 2022-08-23, from https://onlinelibrary.wiley.com/doi/abs/10.1029/2010JA015461 (_eprint: https://onlinelibrary.wiley.com/doi/pdf/10.1029/2010JA015461) doi: 10.1029/2010JA015461

Milan, S. E., Carter, J. A., Sangha, H., Bower, G. E., & Anderson, B. J. (2021). Magnetospheric Flux Throughput in the Dungey Cycle: Identification of Convection State During 2010. *Journal of Geophysical Research: Space Physics*, *126*(2), e2020JA028437. Retrieved 2023-07-13, from https://onlinelibrary.wiley.com/doi/abs/10.1029/2020JA028437 (_eprint: https://onlinelibrary.wiley.com/doi/pdf/10.1029/2020JA028437) doi: 10.1029/2020JA028437

Milan, S. E., Hutchinson, J., Boakes, P. D., & Hubert, B. (2009, July). Influences on the radius of the auroral oval. *Annales Geophysicae*, *27*(7), 2913–2924. Retrieved 2023-07-25, from https://angeo.copernicus.org/articles/27/2913/2009/angeo-27-2913-2009.html (Publisher: Copernicus GmbH) doi: 10.5194/angeo-27-2913-2009

Milan, S. E., Imber, S. M., Fleetham, A. L., & Gjerloev, J. (2023). Solar Cycle and Solar Wind Dependence of the Occurrence of Large dB/dt Events at High Latitudes. *Journal of Geophysical Research: Space Physics*, *128*(4), e2022JA030953. Retrieved 2023-04-17, from https://onlinelibrary.wiley.com/doi/abs/10.1029/2022JA030953 (_eprint: https://onlinelibrary.wiley.com/doi/pdf/10.1029/2022JA030953) doi: 10.1029/2022JA030953

Nagai, T., Fujimoto, M., Saito, Y., Machida, S., Terasawa, T., Nakamura, R., . . . Kokubun, S. (1998, March). Structure and dynamics of magnetic reconnection for substorm onsets with Geotail observations. *Journal of Geophysical Research: Space Physics*, *103*(A3), 4419–4440. Retrieved 2023-03-16, from http://doi.wiley.com/10.1029/97JA02190 doi: 10.1029/97JA02190

Nakai, H., & Kamide, Y. (2003, April). Substorm-associated large-scale magnetic field changes in the magnetotail: a prerequisite for "magnetotail deflation" events. *Annales Geophysicae*, *21*(4), 869–879. Retrieved 2023-07-13, from https://angeo.copernicus.org/articles/21/869/2003/angeo-21-869-2003.html (Publisher: Copernicus GmbH) doi: 10.5194/angeo-21-869-2003

Newell, P. T., & Gjerloev, J. W. (2012). SuperMAG-based partial ring current indices. *Journal of Geophysical Research: Space Physics*, *117*(A5). Retrieved 2022-08-30, from https://onlinelibrary.wiley.com/doi/abs/10.1029/2012JA017586 (_eprint:

https://onlinelibrary.wiley.com/doi/pdf/10.1029/2012JA017586) doi: 10.1029/2012JA017586

Newell, P. T., & Gjerloev, J. W. (2014). Local geomagnetic indices and the prediction of auroral power. *Journal of Geophysical Research: Space Physics*, *119*(12), 9790–9803. Retrieved 2022-08-30, from `https://onlinelibrary.wiley.com/doi/abs/10.1002/2014JA020524` (_eprint: https://onlinelibrary.wiley.com/doi/pdf/10.1002/2014JA020524) doi: 10.1002/2014JA020524

Ngwira, C. M., Pulkkinen, A. A., Bernabeu, E., Eichner, J., Viljanen, A., & Crowley, G. (2015). Characteristics of extreme geoelectric fields and their possible causes: Localized peak enhancements. *Geophysical Research Letters*, *42*(17), 6916–6921. Retrieved 2022-06-10, from `https://onlinelibrary.wiley.com/doi/abs/10.1002/2015GL065061` (_eprint: https://onlinelibrary.wiley.com/doi/pdf/10.1002/2015GL065061) doi: 10.1002/2015GL065061

Ohtani, S. (2021). Revisiting the Partial Ring Current Model: Longitudinal Asymmetry of Ground Magnetic Depression During Geomagnetic Storms. *Journal of Geophysical Research: Space Physics*, *126*(9), e2021JA029643. Retrieved 2023-01-11, from `https://onlinelibrary.wiley.com/doi/abs/10.1029/2021JA029643` (_eprint: https://onlinelibrary.wiley.com/doi/pdf/10.1029/2021JA029643) doi: 10.1029/2021JA029643

Ohtani, S., Ebihara, Y., & Singer, H. J. (2007). Storm-time magnetic configurations at geosynchronous orbit: Comparison between the main and recovery phases. *Journal of Geophysical Research: Space Physics*, *112*(A5). Retrieved 2023-04-11, from `https://onlinelibrary.wiley.com/doi/abs/10.1029/2006JA011959` (_eprint: https://onlinelibrary.wiley.com/doi/pdf/10.1029/2006JA011959) doi: 10.1029/2006JA011959

Ohtani, S., Gjerloev, J., Sorathia, K., & Merkin, V. G. (2022). External and internal causes of the dawnside current wedge formation during geomagnetic storms. In *Fall meeting 2022.*

Ohtani, S., Gjerloev, J. W., Anderson, B. J., Kataoka, R., Troshichev, O., & Watari, S. (2018, November). Dawnside Wedge Current System Formed During Intense Geomagnetic Storms. *Journal of Geophysical Research: Space Physics*, *123*(11), 9093–9109. doi: 10.1029/2018ja025678

Pembroke, A., Toffoletto, F., Sazykin, S., Wiltberger, M., Lyon, J., Merkin, V., & Schmitt, P. (2012, February). Initial results from a dynamic coupled magnetosphere-ionosphere-ring current model. *Journal of Geophysical Research*, *117*(A), A02211. doi: 10.1029/2011ja016979

Pham, K. H., Zhang, B., Sorathia, K., Dang, T., Wang, W., Merkin, V., ... Lyon, J. (2022). Thermospheric Density Perturbations Produced by Traveling Atmospheric Disturbances During August 2005 Storm. *Journal of Geophysical Research: Space Physics*, *127*(2), e2021JA030071. Retrieved 2022-07-22, from `https://onlinelibrary.wiley.com/doi/abs/10.1029/2021JA030071` (_eprint: https://onlinelibrary.wiley.com/doi/pdf/10.1029/2021JA030071) doi: 10.1029/2021JA030071

Pontius Jr., D. H., & Wolf, R. A. (1990). Transient flux tubes in the terrestrial magnetosphere. *Geophysical Research Letters*, *17*(1), 49–52. Retrieved 2022-06-15, from `https://onlinelibrary.wiley.com/doi/abs/10.1029/GL017i001p00049` (_eprint: https://onlinelibrary.wiley.com/doi/pdf/10.1029/GL017i001p00049) doi: 10.1029/GL017i001p00049

Pulkkinen, A. (2015, November). Geomagnetically Induced Currents Modeling and Forecasting. *Space Weather*, *13*(1), 734 – 736. doi: 10.1002/2015sw001316

Pulkkinen, A., Bernabeu, E., Thomson, A., Viljanen, A., Pirjola, R., Boteler, D., … MacAlester, M. (2017, July). Geomagnetically induced currents: Science, engineering, and applications readiness. *Space Weather*, *15*(7), 828 – 856. doi: 10.1002/2016sw001501

Pulkkinen, A., Kuznetsova, M., Ridley, A., Raeder, J., Vapirev, A., Weimer, D., … Chulaki, A. (2011, February). Geospace Environment Modeling 2008–2009 Challenge: Ground magnetic field perturbations. *Space Weather*, *9*(2), n/a – n/a. Retrieved from https://agupubs.onlinelibrary.wiley.com/doi/full/10.1029/2010SW000600 doi: 10.1029/2010sw000600

Rastätter, L., Tóth, G., Kuznetsova, M. M., & Pulkkinen, A. A. (2014). CalcDeltaB: An efficient postprocessing tool to calculate ground-level magnetic perturbations from global magnetosphere simulations. *Space Weather*, *12*(9), 553–565. doi: 10.1002/2014sw001083

Robinson, R. M., Vondrak, R. R., Miller, K., Dabbs, T., & Hardy, D. (1987). On calculating ionospheric conductances from the flux and energy of precipitating electrons. *Journal of Geophysical Research: Space Physics*, *92*(A3), 2565–2569. doi: 10.1029/ja092ia03p02565

Roelof, E. C. (1989, January). Remote sensing of the ring current using energetic neutral atoms. *Advances in Space Research*, *9*(12), 195–203. Retrieved 2023-02-10, from https://www.sciencedirect.com/science/article/pii/0273117789903293 doi: 10.1016/0273-1177(89)90329-3

Roelof, E. C., C:son Brandt, P., & Mitchell, D. G. (2004, January). Derivation of currents and diamagnetic effects from global plasma pressure distributions obtained by IMAGE/HENA. *Advances in Space Research*, *33*(5), 747–751. Retrieved 2023-02-10, from https://www.sciencedirect.com/science/article/pii/S0273117703006380 doi: 10.1016/S0273-1177(03)00638-0

Rostoker, G. (2013, March). Some Observational Constraints for Substorm Models. In J. R. Kan, T. A. Potemra, S. Kokubun, & T. Iijima (Eds.), *Geophysical Monograph Series* (pp. 61–72). Washington, D. C.: American Geophysical Union. Retrieved 2023-03-15, from http://doi.wiley.com/10.1029/GM064p0061 doi: 10.1029/GM064p0061

Runov, A., Angelopoulos, V., Weygand, J. M., Artemyev, A. V., Beyene, F., Sergeev, V., … Henderson, M. G. (2022, September). Thin Current Sheet Formation and Reconnection at X $\sim$ -10 R_E During the Main Phase of a Magnetic Storm. *Journal of Geophysical Research (Space Physics)*, *127*(9), e30669. doi: 10.1029/2022JA030669

Schillings, A., Palin, L., Opgenoorth, H. J., Hamrin, M., Rosenqvist, L., Gjerloev, J. W., … Barnes, R. (2022). Distribution and Occurrence Frequency of dB/dt Spikes During Magnetic Storms 1980–2020. *Space Weather*, *20*(5), e2021SW002953. Retrieved 2022-07-12, from https://onlinelibrary.wiley.com/doi/abs/10.1029/2021SW002953 (_eprint: https://onlinelibrary.wiley.com/doi/pdf/10.1029/2021SW002953) doi: 10.1029/2021SW002953

Sciola, A., Merkin, V. G., Sorathia, K., Gkioulidou, M., Bao, S., Toffoletto, F. R., … Ukhorskiy, A. (2023, June). *The contribution of plasma sheet bubbles to stormtime ring current buildup and evolution of the energy composition* (preprint). Preprints. Retrieved 2023-08-11, from https://essopenarchive.org/users/617933/articles/643144-the-contribution-of-plasma-sheet-bubbles-to-stormtime-ring-current-buildup-and-evolution-of-the-energy-composition?commit=6573b51f10cfcf437a9110c830862aeb1a905bfa doi: 10.22541/essoar.168677230.00750251/v1

Sibeck, D. G., McEntire, R. W., Lui, A. T. Y., Lopez, R. E., Krimigis, S. M., Decker, R. B., … Potemra, T. A. (1987, November). Energetic magnetospheric ions at the dayside magnetopause: Leakage or merging? *Journal of*

Geophysical Research: Space Physics, *92*(A11), 12097 – 12114. Retrieved from `http://onlinelibrary.wiley.com/doi/10.1029/JA092iA11p12097/full` doi: 10.1029/ja092ia11p12097

Singer, H., Matheson, L., Grubb, R., Newman, A., & Bouwer, D. (1996). Monitoring space weather with the GOES magnetometers. In E. R. Washwell (Ed.), *Goes-8 and beyond* (Vol. 2812, pp. 299 – 308). SPIE. Retrieved from `https://doi.org/10.1117/12.254077` doi: 10.1117/12.254077

Sitnov, M. I., Tsyganenko, N. A., Ukhorskiy, A. Y., & Brandt, P. C. (2008). Dynamical data-based modeling of the storm-time geomagnetic field with enhanced spatial resolution. *Journal of Geophysical Research: Space Physics*, *113*(A7). Retrieved 2023-02-10, from `https://onlinelibrary.wiley.com/doi/abs/10.1029/2007JA013003` (_eprint: https://onlinelibrary.wiley.com/doi/pdf/10.1029/2007JA013003) doi: 10.1029/2007JA013003

Sorathia, K. (2023, Aug). Multiscale magnetosphere-ionosphere coupling during stormtime: A case study of the dawnside current wedge [dataset]. *Zenodo*. Retrieved from `https://zenodo.org/record/8178574` doi: 10.5281/ZENODO.8178574

Sorathia, K. A., Merkin, V. G., Panov, E. V., Zhang, B., Lyon, J. G., Garretson, J., … Wiltberger, M. (2020). Ballooning-Interchange Instability in the Near-Earth Plasma Sheet and Auroral Beads: Global Magnetospheric Modeling at the Limit of the MHD Approximation. *Geophysical Research Letters*, *47*(14). doi: 10.1029/2020gl088227

Stephens, G. K., Sitnov, M. I., Ukhorskiy, A. Y., Roelof, E. C., Tsyganenko, N. A., & Le, G. (2016, January). Empirical modeling of the storm time innermost magnetosphere using Van Allen Probes and THEMIS data: Eastward and banana currents. *Journal of Geophysical Research: Space Physics*, *121*(1), 157 – 170. Retrieved from `https://agupubs.onlinelibrary.wiley.com/doi/epdf/10.1002/2015JA021700` doi: 10.1002/2015ja021700

Sugiura, M. (1961). *A Study of the Morphology of Geomagnetic Storms*. Geophysical Institute of the University of Alaska. (Google-Books-ID: En_WeO5JGPUC)

Toffoletto, F., Sazykin, S., Spiro, R., & Wolf, R. (2003, April). Inner magnetospheric modeling with the Rice Convection Model. *Space Science Reviews*, *107*(1-2), 175 – 196. doi: 10.1023/a:1025532008047

Untiedt, J., & Baumjohann, W. (1993). Studies of polar current systems using the IMS Scandinavian magnetometer array. *Space Science Reviews*, *63*(3-4), 245–390. Retrieved 2023-02-28, from `http://link.springer.com/10.1007/BF00750770` doi: 10.1007/BF00750770

Vasyliunas, V. M. (1970). Mathematical Models of Magnetospheric Convection and its Coupling to the Ionosphere. In B. M. McCormac (Ed.), *Particles and Fields in the Magnetosphere* (pp. 60–71). Dordrecht: Springer Netherlands. doi: 10.1007/978-94-010-3284-1_6

Waters, C. L., Anderson, B. J., Green, D. L., Korth, H., Barnes, R. J., & Vanhamäki, H. (2020). Science Data Products for AMPERE. *Ionospheric Multi-Spacecraft Analysis Tools*, *1*(A5), 141. doi: 10.1007/978-3-030-26732-2_7

Wing, S., Ohtani, S.-i., Newell, P. T., Higuchi, T., Ueno, G., & Weygand, J. M. (2010, December). Dayside field-aligned current source regions: DAYSIDE FIELD-ALIGNED CURRENT SOURCE REG. *Journal of Geophysical Research: Space Physics*, *115*(A12), n/a–n/a. Retrieved 2023-02-28, from `http://doi.wiley.com/10.1029/2010JA015837` doi: 10.1029/2010JA015837

Wolf, R. A. (1983). Solar-Terrestrial Physics, Principles and Theoretical Foundations Based Upon the Proceedings of the Theory Institute Held at Boston College, August 9–26, 1982. *Astrophysics and Space Science Library*, 303–368. doi: 10.1007/978-94-009-7194-3_14

Zhang, B., Sorathia, K. A., Lyon, J. G., Merkin, V. G., Garretson, J. S., & Wiltberger, M. (2019, September). GAMERA: A Three-dimensional Finite-volume MHD Solver for Non-orthogonal Curvilinear Geometries. *The Astrophysical Journal Supplement Series*, *244*(1), 20. doi: 10.3847/1538-4365/ab3a4c

Zou, Y., Dowell, C., Ferdousi, B., Lyons, L. R., & Liu, J. (2022). Auroral Drivers of Large dB/dt During Geomagnetic Storms. *Space Weather*, *20*(11), e2022SW003121. Retrieved 2023-07-13, from `https://onlinelibrary.wiley.com/doi/abs/10.1029/2022SW003121` (_eprint: https://onlinelibrary.wiley.com/doi/pdf/10.1029/2022SW003121) doi: 10.1029/2022SW003121

Østgaard, N., Mende, S. B., Frey, H. U., Gladstone, G. R., & Lauche, H. (2003). Neutral hydrogen density profiles derived from geocoronal imaging. *Journal of Geophysical Research: Space Physics (1978–2012)*, *108*(A7). doi: 10.1029/2002ja009749